Title:

A slow 5-HT1AR-mediated recurrent inhibitory network in raphe computes contextual value through synaptic facilitation

Short title:
Winner-take-all computations and sharp behavioral state transitions

Authors:
Michael B. Lynn[1], Sean Geddes[1], Mohamad Chahrour[1], Sébastien Maillé[1], Emerson Harkin[1], Érik Harvey-Girard[1], Samir Haj-Dahmane[6], Richard Naud[1,3,4,5], Jean-Claude Béïque[1,2,3,4*]

Affiliations:
[1]Department of Cellular and Molecular Medicine, University of Ottawa, Ottawa, ON K1H 8M5, Canada
[2]Canadian Partnership for Stroke Recovery, University of Ottawa, Ottawa, ON K1H 8M5, Canada
[3]Centre for Neural Dynamics, University of Ottawa, Ottawa, ON K1H 8M5, Canada
[4]Brain and Mind Research Institute, University of Ottawa, ON K1H 8M5, Canada
[5]Department of Physics, STEM Complex, Room 336, 150 Louis Pasteur Private, University of Ottawa, Ottawa, ON K1N 6N5, Canada
[6]Department of Pharmacology and Toxicology, University at Buffalo, Buffalo, NY 14203, U.S.A.

Corresponding Authors:

* Correspondence: jbeique@uottawa.ca (J.-C. B.).

Abstract

Serotonin (5-HT) neurons in the dorsal raphe nucleus (DRN) receive a diverse constellation of long-range synaptic inputs, yet unifying principles of local circuitry and its dynamics are largely unknown - a crucial component of understanding how 5-HT output controls behavior. Here, we developed a formalism bridging optogenetic, electrophysiological, computational and behavioral strategies to reveal how the dynamics of local circuitry in DRN control the expression of reward associations. Using long-range input from lateral habenula (LHb) to interrogate functional DRN circuitry, we uncover 5-HT1A receptor-mediated local recurrent connections between 5-HT neurons, refuting classical theories of autoinhibition by 5-HT1A receptors. These inhibitory 5-HT connections were slow, stochastic, strongly facilitating, and gated spike output of 5-HT neurons. Targeted physiology and modeling approaches revealed that these functional connectivity features collectively support the emergence of a paradoxical excitation-driven inhibition in response to high frequency LHb activation, and of a winner-take-all computation over protracted timescales. *In vivo,* we found that optogenetic activation of LHb inputs to DRN transiently disrupted expression of a reward-conditioned response in an auditory conditioning task. In accordance with quantitative model predictions, this disruption occurred exclusively at the conjunction of high frequency LHb activation and high predicted reward value, and was not due to a modulation of the underlying reward association. Thus, we propose that recurrent dynamics in the DRN support a contextual value computation, where stable learned associations are integrated with dynamic environmental inputs to support sharp behavioral state transitions in changing environments.

Keywords: Serotonin; dorsal raphe nucleus; habenula; recurrent dynamics; short-term plasticity; winner-take-all; learned associations; value computation.

Introduction

Animals show a remarkable ability to adapt their behavioral state to environmental contexts. These adaptations can exhibit nonlinear relationships with environmental parameters that appear otherwise graded. For instance, various stress factors affect behavioral motivation positively at low levels but negatively at high levels (Yerkes-Dodson law; Yerkes and Dodson 1908; Broadhurst 1957 ; Salehi et al. 2010). While coordinated behavioral regulation has been associated with multiple neuromodulatory systems (Eriksson et al., 2017), it remains a challenge to identify how defined behavioral features emerge from specific network computations occurring in those neuromodulatory systems. Overall, neural computations implementing sharp behavioral state transitions from linear and graded neural representations of stimuli remain poorly characterized.

The serotonergic dorsal raphe nucleus (DRN) is a heterogeneous midbrain nucleus which regulates mood and behavior through its widespread efferent innervation (Dorocic et al., 2014; Weissbourd et al., 2014). The coding features of DRN 5-HT neurons still remain largely elusive, although recent studies have shown that they respond to environmental variables such as reward and threat (Cohen et al., 2015; Li et al., 2016; Zhong et al., 2017; Seo et al., 2019), making them suited to supervise behavioral policies based on internal representations of environmental contexts. Moreover, the DRN has been linked to a diverse range of mood-related states such as aggression (Takahashi et al., 2015) and patience (Miyazaki et al., 2014; Miyazaki et al., 2018; Miyazaki et al., 2020), as well as to the etiology in depressive and anxiety disorders (Graeff et al., 1996; Warden et al., 2012). DRN microcircuits are composed of multiple intermingled cell types, including dopaminergic, glutamatergic, serotonergic and GABAergic neurons, organized into functionally distinct modules (Ren et al., 2018). However, the precise rules by which these circuits process incoming information to ultimately provide instructive cues to regulate behavior are largely unknown.

One major source of input to the DRN is from the lateral habenula (LHb), which provides monosynaptic excitatory drive to 5-HT neurons (Zhou et al., 2017). LHb neurons fire in response to punishments, reward omissions and threat by phasic, high-frequency discharges, providing a neural scaffold for valence-based behavioral modification and learning (Matsumoto & Hikosaka, 2009; Proulx et al., 2014; Bromberg-Martin & Hikosaka, 2011; Lecca et al., 2020; Amo et al., 2014; Yang et al., 2018). Recent work has suggested that both the raphe and habenula regulate behavioral policy over long timescales by modifying internal representations (Marques et al., 2020). How incoming synaptic inputs from LHb, carrying graded threat information over milliseconds, are processed by DRN microcircuits into an internal state representation that persists over longer timescales to influence behavioral policy is currently unknown.

Here, we developed a synthesis of optogenetic, electrophysiological, computational and behavioral strategies to elucidate key principles by which local DRN microcircuits enact computations. Using long-range inputs from LHb to interrogate DRN functional circuitry under ethologically meaningful drive, we uncovered an unexpected slow inhibitory conductance reflecting local recurrent connections between 5-HT neurons. These recurrent connections, mediated by inhibitory 5-HT_{1A} receptors (5-HT_{1A}Rs), were slow, highly facilitating, and modulated spiking output of the circuit. We provide a simple, unified model of the complex short-term dynamics of these recurrent serotonin connections, which, along with biophysically grounded modeling, predicts a sharp transition from net excitation to excitation-driven inhibition, as well as winner-take-all dynamics between long-range inputs to ensembles in DRN. These findings suggest operating principles for interactions between heterogeneous modules within

DRN. The behavioral consequences of these computations were examined using a head-fixed auditory classical conditioning task, revealing that activating LHb inputs to DRN produced reward value-dependent effects on reward anticipation exclusively at high photostimulation frequencies quantitatively predicted by our network modeling. Our results provide a comprehensive description of a novel circuit motif in DRN, redefine the role of a key serotonin receptor subtype, and provide key algorithmic insights into how environmental threats can be non-linearly processed and thresholded by a mood-related microcircuit to ultimately drive sharp transitions between competing behavioral policies.

Results

Excitatory monosynaptic LHb inputs to DRN trigger a frequency-dependent indirect inhibition

As a first step towards uncovering organizing principles of microcircuitry within DRN, we activated LHb, a strong long-range input to DRN, and probed neural responses. We utilized a SERT-CRE-tdTomato mouse line for whole-cell electrophysiological recordings from genetically identified 5-HT neurons, validating this approach with immunohistochemical staining (Fig. S1A-D; 98.4% overlap between TPH2 and tDtomato expression). Upon bilateral injection of AAV-GFP in LHb, we observed dense LHb axon density in DRN (Fig. S2A) consistent with recent work (Zhou et al., 2017). Next, we injected AAV-ChR2(H134R)-mCherry bilaterally into LHb of SERT-CRE-tdTomato mice (Fig. 1A and Fig. S1E, see Methods). Photostimulation induced strong and reliable action potentials in LHb neurons which were qualitatively similar to those following current step injections (Fig. S2B-C). Recording from identified DRN 5-HT neurons in the voltage-clamp configuration (Fig. 1C-D) showed that single brief (1-3 ms) pulses of blue light triggered synaptic release of glutamate that activated AMPARs (Fig. 1E; V_m=-70 mV) and NMDARs (Fig. 1F; V_m=+40mV). LED-stimulated glutamate release was blocked by TTX and rescued by the K+ channel blocker 4-AP (Fig. 1G), indicating that LHb makes monosynaptic contacts with DRN 5-HT neurons. These excitatory inputs from LHb were capable of driving 5-HT neurons to spike (Fig. 1H). Thus, LHb afferents directly excite 5-HT neurons, consistent with previous reports (Zhou et al., 2017). While habenula-driven feedforward inhibition onto 5-HT neurons has been previously reported (Zhou et al., 2017), we observed no evidence of optically triggered IPSCs in our recording conditions (n=116 neurons). This stands in stark contrast to our previous finding of prominent feedforward inhibition onto 5-HT cells triggered by prefrontal cortex inputs to the DRN (Geddes et al., 2016).

LHb neurons can discharge either acutely at high rates following threatening stimuli, or at lower sustained levels (Matsumoto & Hikosaka, 2009; Yang et al., 2018, Dolzani et al., 2016, Amo et al., 2014). To explore how such variable input patterns, carrying graded threat information, are processed and potentially parsed by DRN microcircuits, we delivered trains of optical stimuli at a range of frequencies consistent with previously reported *in vivo* phasic habenular responses (Amo et al., 2014). Train stimulation at 10Hz or 20Hz, surprisingly, triggered the appearance of a delayed outward current lasting hundreds of milliseconds, following the initial monosynaptic EPSCs (Fig. 1I). The overall kinetics of this protracted current, as well as its underlying rectifying I-V curve displaying a reversal potential at ~-77mV (Fig. 1J), suggest the involvement of a G-protein inwardly rectifying potassium (GIRK) channel (Newberry & Nicoll, 1984). While several G-protein coupled receptor subtypes couple to GIRK channels, the inhibitory 5-HT receptor of the 5-HT_{1A} subtype are expressed at high level in DRN 5-HT neurons (Pazos & Palacios, 1985) and were thus reasonable candidates. Bath application of

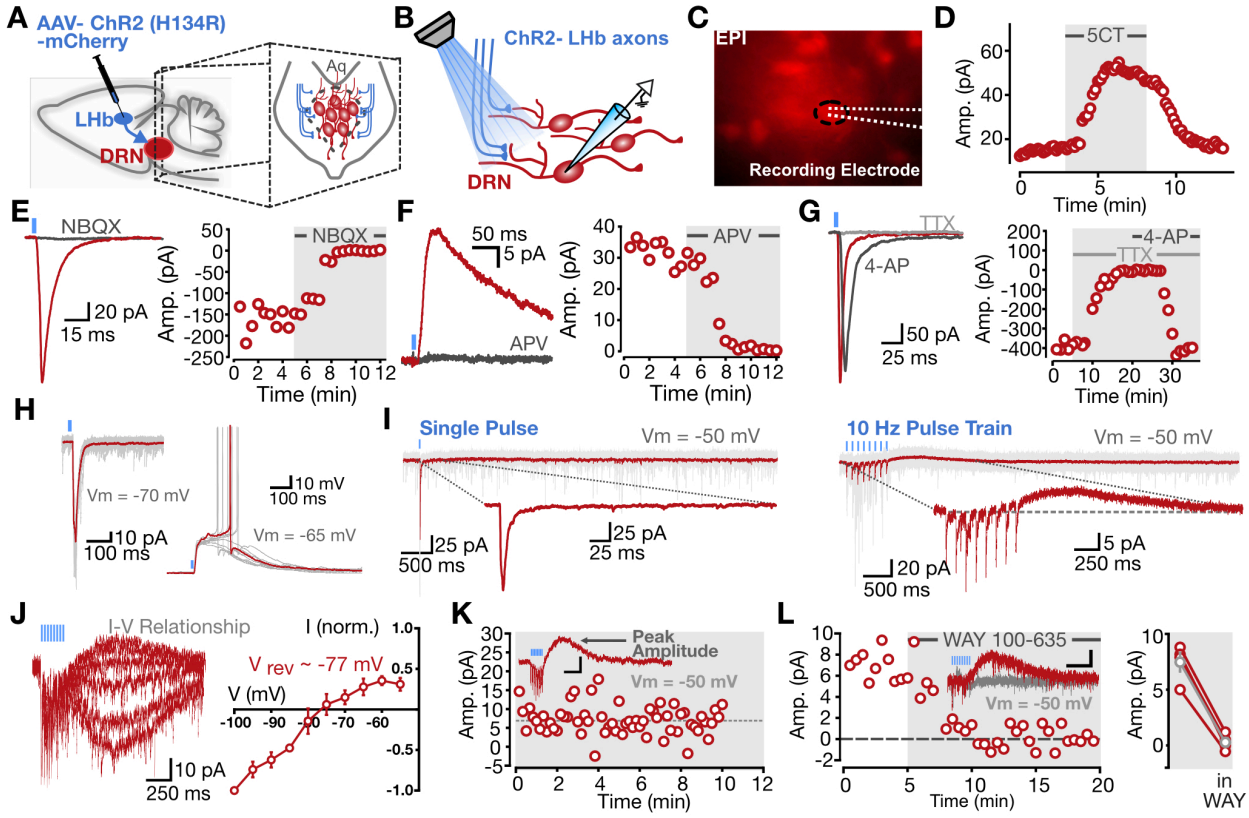

Figure 1: Habenula input to raphe triggers direct excitation and heterosynaptic inhibition in 5-HT neurons. **(A-B)** Schematic of experimental approach. **(C)** Epifluorescent image of tdTomato-positive 5-HT neurons. **(D)** Application of 5-CT (100nM) triggered a transient increase in holding potential. **(E)** Single pulses of light at Vm=-70mV triggered EPSCs (left) which were abolished by application of NBQX (10uM, right). **(F)** At Vm=+40mV, single pulses of light triggered EPSCs (left) which were abolished by application of APV (50uM, right). **(G)** Application of TTX (1uM) blocked EPSCs at Vm=-70mV, while subsequent application of 4-AP (1mM) recovered the current. **(H)** Voltage-clamp recordings of ChR2-EPSCs (Vm = -70 mV) and spiking behavior in response to presynaptic activation. **(I)** Representative 5-HT neuron responses to single pulses of light (left) and pulse trains at 10Hz (right). **(J)** Representative traces of the current-voltage (I-V) relationship of the delayed outward current (left) and group data (right, n=3 neurons, mean +/- SE) **(K)** Representative timecourse of peak amplitude stability over time. **(L)** Representative traces and timecourse showing the blockade of the outward current by WAY 100-635 (400 nM; left). Population data presented in a scatter-line plot (right, Pre-WAY, 7.47 +/- 0.8; Post-WAY, 0.28 +/- 0.4; n = 4 neurons; p = 0.001; paired two-sided t-test).

184 the 5-HT_{1A}R antagonist WAY100-635 abolished the outward current triggered by burst
185 activation of LHb axons in the DRN without influencing the light-induced EPSCs (Fig. 1L).
186 Together, these results demonstrate that LHb input to DRN 5-HT neurons trigger a rapid
187 monosynaptic glutamatergic-mediated excitation followed by a slower, 5-HT_{1A}R-mediated
188 inhibition.
189
190 *DRN 5-HT neurons are organized in a recurrent inhibitory network*
191 We next sought to identify the cellular and network underpinnings of this non-canonical
192 mixed excitation/inhibition response, initially focusing on the protracted 5-HT_{1A}R-mediated
193 inhibition. A dominant and well-accepted model posits that 5-HT1ARs are autoreceptors. In this
194 model, individual 5-HT neurons, upon firing, limit their own excitability through the dendritic
195 release of 5-HT (Maxwell et al., 1983; Ridet et al., 1994; Bunin & Wightmann, 1998), which
196 activates these so-called inhibitory somatodendritic 5-HT_{1A} autoreceptors in an autocrine fashion
197 (Gozlan et al., 1983; Weissmann-Nanopoulos et al., 1985; Pineyro & Blier, 1999). This
198 canonical autoreceptor model is nonetheless difficult to reconcile with our observations that train
199 activation of LHb inputs triggered 5-HT_{1A}R-mediated outward currents in nonspiking, voltage-
200 clamped 5-HT neurons (Fig. 1I,J), or in 5-HT neurons receiving no functional excitatory LHb
201 inputs (Fig. S2D-E). We therefore next sought to experimentally disambiguate the autoreceptor
202 hypothesis from the alternative hypothesis that DRN 5-HT neurons are organized in a recurrent
203 inhibitory network architecture (Fig. 2A).
204 We first reasoned that if 5-HT_{1A}Rs were indeed autocrine inhibitory autoreceptors,
205 evoked spikes from a single 5-HT neuron should elicit a 5-HT1AR-mediated inhibition in the
206 same isolated neuron, contributing to the post-spike afterhyperpolarization (AHP) commonly
207 observed in 5-HT neurons (Vandermaelen & Aghajanian, 1983). Whole-cell recordings,
208 however, revealed that the post-spiking AHP triggered by current injection was insensitive to
209 application of the 5-HT_{1A}R antagonist WAY100-635 (Fig. 2B-D), yet fully abolished by
210 application of the SK channel blocker apamin (Fig. 2E-H). The absence of autocrine effects on
211 the AHP could be explained by the small number of action potentials emitted in current-clamp
212 experiments. Voltage-clamp experiments showed that the robust outward current that followed
213 long, constant, depolarizing voltage steps in 5-HT neurons was also sensitive to apamin, but not
214 to WAY100-635 (Fig. S3). Together, these experiments failed to support the autocrine function
215 for 5-HT_{1A}Rs on 5-HT neurons, instead implicating calcium-activated potassium channels of the
216 SK subtype in generating the AHP in 5-HT neurons.
217 To begin exploring the alternative possibility of a recurrent network between 5-HT
218 neurons in DRN, we injected a fluorescent dextran retrograde tracer into acute DRN slices to
219 visualize possible local recurrent connectivity (Trinh et al., 2016; see Methods). These
220 experiments revealed the presence of genetically-confirmed 5-HT neuron somas in DRN
221 >150um away from the purported site of injection (Fig S4). By suggesting the presence of local
222 connectivity between DRN 5-HT neurons, these experiments prompted us to examine this
223 possibility more rigorously. We thus designed a series of targeted optogenetic strategies based on
224 viral transduction of 5-HT neurons with a Cre-dependent AAV ChETA-YFP in SERT-
225 Cre:tdTomato mice (Fig. S5A, see Methods). *Ex vivo* slice recordings from DRN 5-HT neurons
226 co-expressing tdTomato and YFP-tagged ChETA opsin (Fig. S5B-C) showed that LED
227 stimulation induced robust inward photocurrents/depolarizations that induced spiking reliably up
228 to ~20 Hz (Fig. S5D-E). Train photostimulation of all transduced 5-HT neurons triggered a
229 robust inhibitory 5-HT_{1A}R conductance (Fig. S5F-G). We then reasoned that neuronal spiking

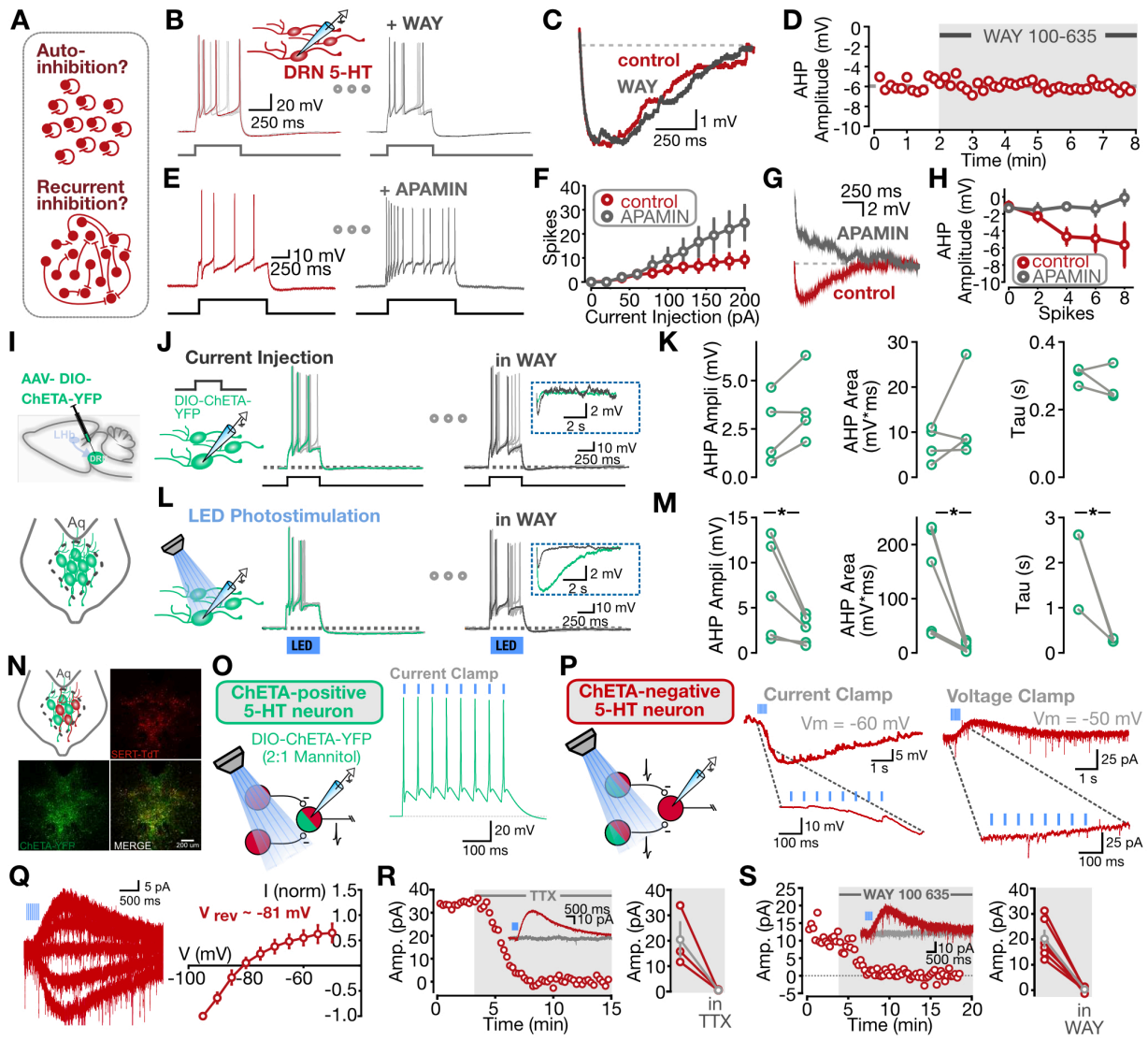

Figure 2: 5-HT neurons in raphe are organized in a recurrent inhibitory network. **(A)** Two hypothesized mechanisms of 5-HT1AR-based signaling in raphe. **(B)** Representative traces of spiking in response to direct current injection before and after WAY 100-635 application. **(C)** Direct comparison of AHP before and after application of WAY 100-635. **(D)** Representative scatter plot showing no change in the AHP amplitude with bath application of WAY 100-635. **(E)** Representative traces of spiking in response to direct current injection before and after APAMIN application. **(F)** Relationship between current injection strength and evoked spikes, in the presence or absence of APAMIN (n=3 neurons, mean +/- SE) **(G)** Direct comparison of AHP before and after application of APAMIN. **(H)** Relationship between spike number and AHP amplitude, in the presence or absence of APAMIN (n=3 neurons, mean +/- SE). **(I)** Schematic of local optogenetic experimental approach. **(J)** Representative traces from CHETA-expressing 5-HT neurons showing current step-driven spiking before (green) and after (black) bath application of WAY100-635. **(K)** Quantification of AHP statistics for control and WAY100-635 conditions (AHP amplitude, p=0.96, n=4 neurons; AHP area, p=0.85, n=4 neurons; AHP tau, p=0.09, n=3 neurons; paired two-sided t-tests). **(L)** Representative traces from CHETA-

expressing 5-HT neurons showing photostimulation-driven spiking before (green) and after (black) bath application of WAY100-635. **(M)** Quantification of AHP statistics for control and WAY100-635 conditions (AHP amplitude, p=0.03, n=5 neurons; AHP area, p=0.03, n=5 neurons; AHP tau, p=0.02, n=3 neurons; paired two-sided t-tests). **(N)** Schematic and confocal images of sparse local optogenetic approach (AAV-DIO-CHETA-YFP diluted in mannitol 2:1). **(O)** While recording from an opsin-expressing neuron, brief optical stimulation could reliably elicit spiking behavior. **(P)** While recording from a non-opsin-expressing serotonergic neuron, photostimulation at 20Hz produced an inhibitory current; note the absence of direct photocurrents. **(Q)** Representative traces of the current-voltage (I-V) relationship of the inhibitory current (left) and group data (right, n=5 neurons, mean +/- SE) **(R)** Representative traces and timecourse of TTX (1uM) bath application (left) and group data (right; n=3 neurons; grey average trace: mean +/- SE). **(S)** Representative traces and timecourse of WAY100-635 (400nM) bath application (left) and group data (right; n=6 neurons; grey average trace: mean +/- SE).

230 induced by photostimulating CHETA-expressing 5-HT neurons should reveal an additive 5-
231 $HT_{1A}R$ mediated component of the resultant AHP in the recorded neuron if DRN 5-HT neurons
232 were indeed interconnected in a recurrent inhibitory network. To test this, we cross-calibrated
233 single-cell direct current injections and LED intensity such that both methods independently
234 triggered spiking of similar frequency (Fig. 2J and 2L). While the spiking triggered by direct
235 current injections induced a strong and highly reliable AHP in these neurons (*i.e.,* tdTomato and
236 YFP-tagged ChETA-positive) that was not affected by the 5-$HT_{1A}R$ antagonist WAY100-635
237 (Fig. 2K-L), the spiking triggered by LED photostimulation of the entire DRN network induced a
238 substantially larger AHP, and the additional component was blocked by WAY100-635 (Fig. 2N).
239 These results fail to support the autocrine hypothesis of 5-$HT_{1A}R$ function, and rather provide
240 evidence that 5-HT neurons are organized in a recurrent inhibitory network, communicating via
241 5-$HT_{1A}R$ receptors.
242 In principle, however, it is possible that LED illumination depolarized poorly clamped
243 distal 5-HT dendrites, which could release 5-HT to activate 5-$HT_{1A}R$ in an autocrine fashion. To
244 account for this possibility, we tested one final prediction of the recurrent network hypothesis;
245 namely, that a 5-$HT_{1A}R$-dependent inhibitory conductance should be detected in non-
246 photostimulated 5-HT neurons when other 5-HT neurons in the surrounding network are
247 photostimulated. To directly test this, we implemented an AAV-CHETA-YFP transduction
248 strategy (mannitol dilution, see Methods) in the DRN of SERT-CRE-tdTomato mice (Fig. 2O) to
249 achieve sparse, mosaic-like expression of ChETA-YFP in 5-HT neurons. This allowed us to
250 obtain visually targeted recordings either from ChETA-expressing 5-HT neurons (*i.e.,* YFP and
251 tdTomato expressing neurons; reliable optically driven spiking in Fig. 2P) or non ChETA-
252 expressing 5-HT neurons (*i.e.*, YFP-negative, tdTomato-positive 5-HT neurons). Targeted
253 recordings from non CHETA-expressing 5-HT neurons revealed that high-frequency LED
254 photostimulation, which directly drives the surrounding network but not the recorded neuron,
255 induced delayed strongly rectifying outward currents (Fig. 2Q) which were blocked by TTX and
256 by WAY 100-635 (Fig. 2R-T). Taken together, these anatomical and optogenetic data strongly
257 support the existence of an unsuspected recurrent inhibitory network in DRN, consisting of 5-HT
258 neurons communicating via 5-$HT_{1A}Rs$ over long timescales.
259
260 *A quantitative description of release dynamics at 5-$HT_{1A}R$-mediated recurrent connections*
261 We next parametrized a number of key functional features of the 5-HT synapses between
262 DRN 5-HT neurons using the 5-$HT_{1A}R$ – and GIRK-mediated hyperpolarization as a reporter of
263 5-HT release. Train optogenetic stimulation (20Hz, 8 pulses) of 5-HT neurons triggered a 5-
264 $HT_{1A}R$ conductance that peaked approximately 400 ms following the end of the train (392.6 ±
265 106.9ms) and that slowly decayed (2.1 ± 0.46s). Varying the number of light pulses delivered at
266 20Hz revealed a relationship between pulse number and postsynaptic conductance that was
267 almost linear, indicating that 5-$HT_{1A}R$ coupling to GIRK channels can follow multiple
268 successive activation by endogenous 5-HT with limited desensitization (Fig. S6B-C). To infer
269 presynaptic release dynamics, we next calculated the response variance as a function of pulse
270 number, finding virtually no change in variance despite changes in amplitude (Fig. S6D). While
271 such dynamics are consistent with deterministic neurotransmitter release (*i.e.,* P_{rel} ~1; see
272 Methods for full details), artefactual inflation of presynaptic release probability has previously
273 been reported for optogenetic synaptic terminal activation (Zhang & Oertner, 2007). These
274 results nonetheless outline the timecourse of a GIRK- and 5-$HT_{1A}R$ -mediated synapse, and
275 indicate that postsynaptic receptor binding follows quasi-linearly presynaptic release.

To monitor 5-HT presynaptic release dynamics in the DRN circumventing the confound brought about by optogenetic stimulation, we next recorded DRN 5-HT neurons while electrically stimulating nearby serotonergic fibers with a bipolar concentric electrode (Fig. 3A). A cocktail of synaptic blockers was bath-applied to isolate serotonergic transmission (Fig. 3A, see Methods). High-frequency electrical stimulation readily triggered a 5-HT_{1A}R -mediated outward current with a similar time course to that induced by LED stimulation (Fig. 3B). We next delivered isolated electrical pulses under a low-intensity minimal stimulation regime (*i.e.,* activating small numbers of individual 5-HT synapses) while monitoring 5-HT_{1A}R -mediated currents. These recordings showed instances of clear successes (~5 pA) and failures (Fig. 3C) of 5-HT release, consistent with small numbers of 5-HT synapses each exhibiting a release probability < 1. Fig. 3D depicts the distribution of event charges plotted alongside neuron-specific control distributions (obtained from integrating an equivalent duration of noise; see Methods). The bimodal event distribution, exhibiting a left peak overlapping with the noise distribution, is consistent with probabilistic 5-HT transmission.

We next examined the short-term dynamics of these probabilistic 5-HT synapses by delivering electrical stimulation trains at higher (non-minimal) intensities with a fixed pulse number (8) and variable frequency (Fig. 3E). A synapse with no short-term dynamics should exhibit identical responses over a range of input frequencies if pulse number is fixed. However, while 1 Hz stimulation produced a notably weak response, higher frequencies of 10 Hz and 20 Hz elicited progressively larger inhibitory currents (Fig. 3E-F). To directly compare these protracted responses, which displayed rise-times and peak amplitudes that were highly dependent on stimulus parameters, we employed a z-score based metric of total charge. Briefly, we computed the total charge evoked by each stimulus train, and compared this with a surrogate noise distribution constructed by performing the same integration on an equivalent duration of baseline recording (pre-stimulation, computed within the same neuron, adjusted for each stimulation regime; Fig. 3G, See Methods). While low-frequency (1 Hz) stimuli did not produce responses significantly different from the surrogate noise distribution, high-frequency (20 Hz) stimuli produced progressively larger responses (Fig. 3G-H), consistent with short-term facilitation. To rule out subthreshold presynaptic summation as a possible confounding factor, these experiments were repeated with increased electrical stimulation strength, which returned qualitatively similar short-term facilitation for these 5-HT connections (Fig. S7). We thus conclude that the protracted 5-HT1R-dependent inhibition exhibits substantial short-term facilitation dynamics at frequencies above 5Hz.

To further quantify the timescale of these short-term synaptic dynamics, we delivered patterned electrical stimulation, starting with classic paired-pulse stimulation experiments. When paired-pulse stimuli were closely spaced (50-200 ms) we observed supralinear summation compared to isolated single pulses; in contrast, paired-pulse intervals of 500 ms and longer produced depressing responses (Fig. 3J-K). This short-term depression observed at timescales of seconds is consistent with previous reports on 5-HT_{1A}R-mediated inhibition (Courtney & Ford, 2016). By comparing the actual evoked charge with the predicted linear summation of isolated single-pulse responses, we were able to directly quantify the dynamics of these recurrent synapses across multiple timescales (Fig. 3L). Together, these results indicate that the short-term dynamics of these 5-HT synapses are dominated by strong short-term facilitation at short intervals, transitioning to mild depression at timescales > 500 ms.

To examine meta-dynamic features of these 5-HT synapses, we delivered a second set of patterned electrical stimuli consisting of a paired-pulse stimulation (20 Hz; ISI of 50 ms)

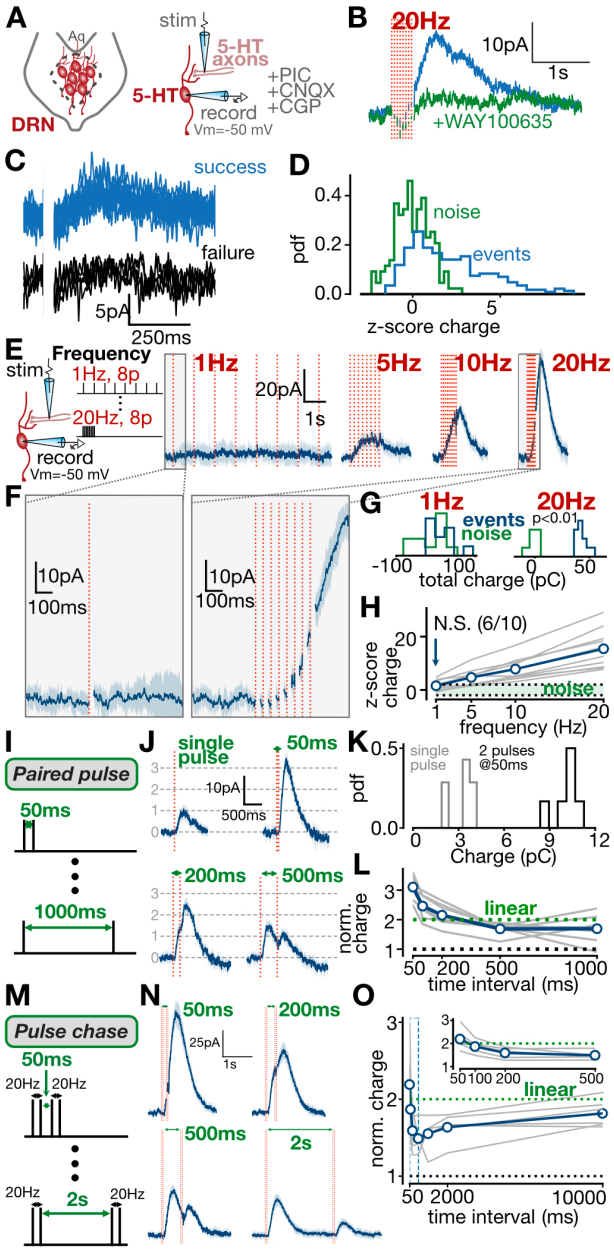

Figure 3: Serotonin release is probabilistic and strongly facilitating at inhibitory recurrent connections. **(A)** Experimental schematic. **(B)** Electrical stimulation at 20Hz evoked an outward current that is blocked by WAY100-635. **(C)** Representative traces depicting responses to low-amplitude electrical stimulation, showing sorted successes and failures from the same neuron. **(D)** Histograms of charge z-score, calculated for post-stimulus events (blue) and an equivalent period of non stimulus-driven noise from the same neuron (black) (n=424 events from 4 neurons). **(E)** Experimental setup for frequency-varying electrical stimulation experiments (left). Representative averaged traces from a single neuron depicting responses to electrical stimulation at various frequencies (right). **(F)** Expanded traces showing responses to 1Hz and 20Hz stimuli. **(G)** Charge histograms for stimulus-driven events and noise (one example neuron; 1Hz: $p>0.05$, 20Hz: $p<0.01$, two-sided t-tests). **(H)** Charge z-score as a function of frequency, with 95% noise C.I shown in green (n=10 neurons, two-sided t-tests for each neuron as in G). **(I)** Paired-pulse electrical stimulation paradigm. **(J)** Representative averaged traces from a single neuron depicting responses to electrical stimulation at various paired-pulse intervals. **(K)** Charge histograms for single-pulse responses and paired-pulse responses at 50ms for one example neuron. **(L)** Post-stimulus charge as a function of paired-pulse time interval (n=7 neurons). Green line depicts linear summation. **(M)** Pulse-chase electrical stimulation paradigm. **(N)** Representative averaged traces from a single neuron depicting responses to pulse-chase electrical stimulation protocol at various temporal intervals. **(O)** Post-stimulus charge as a function of pulse-chase time interval (n=6 neurons). Green line depicts linear summation.

separated from another paired-pulse stimulation by some varying time interval (pulse-chase; Fig. 3M). These experiments revealed, unexpectedly, that the paired-pulse facilitation at 20 Hz is highly dependent on stimulus history over a timescale of seconds. When paired-pulse sets were separated by short intervals, facilitation was observed, but when separated by intervals of >500 ms, the second paired-pulse stimulus elicited notably smaller responses, indicating release meta-dynamics, or a history-dependent change in facilitation (Fig. 3N). Charge quantification metrics, similar to above (see Methods), revealed that this dependence on stimulation history lasted up to 10 seconds (Fig. 3O).

A comprehensive picture of the network computations sustained by this recurrent inhibitory network requires, as an obligatory intermediate step, an accurate quantitative model of the synaptic dynamics described above. Thus, we next developed a mathematical model capturing these ground-truth short-term dynamics of 5-HT synapses. We first fitted the experimentally-derived 5-HT_{1A}R -mediated inhibitory GIRK current with a simple summed exponential model (Fig. 4A). Next, to adequately capture the experimentally-derived short-term dynamics of 5-HT synapses, we fitted our experimental data using a previously described spike-response plasticity model (SRP; Rossbroich et al., 2021; see Methods). Briefly, a presynaptic spiketrain is convolved with a kernel indicating the sign and timescale of synaptic dynamics, passed through a sigmoidal readout, and convolved at each presynaptic spike-time with a postsynaptic event kernel (here, describing a GIRK-mediated current). We used a least-squares approach to fit this model to the experimental paired-pulse data, yielding an optimized short-term plasticity (STP) kernel that showed a short-timescale facilitation and long-timescale depression components (Fig. 4B). The resultant model effectively captured the dynamics of the paired-pulse experimental data across all timescales tested (Fig. 4C). Remarkably, the model was additionally able to describe the meta-facilitation dynamics observed in the pulse-chase experiments, despite not being exposed to this data during fitting – in effect acting as a test set for the model (Fig. 4D). To provide further intuition about this model, we finally conducted simple simulations where presynaptic trains were delivered to single neurons, and the model returned the kinetics and response magnitude of our earlier electrical stimulation experiments (Fig. 4E). Together, these results show that the complex dynamics of 5-HT release in the DRN can be faithfully captured by the SRP model.

Computations performed by a recurrent inhibitory network under excitatory drive

A natural question arising from the highly nonlinear short-term dynamics of 5-HT release observed above is how they contribute to the computations emerging from the DRN recurrent inhibitory network when receiving excitatory drive from long-range inputs. Our results so far show that the habenulo-raphe pathway can be characterized by a balance of direct excitation of 5-HT neurons on short timescales, and frequency-dependent recruitment of recurrent inhibition acting over protracted timescale. Since various connectivity motifs of excitation and inhibition have been ascribed a diverse set of network-level functions (Womelsdorf et al. 2014; Grienberger et al., 2017), we wondered about the potential computations supported by frequency-dependent feedback inhibition with fundamental timescale mismatch.

To investigate the computation carried out by DRN circuits under habenular drive (e.g., threat information), we leveraged our mathematical description of the short-term plasticity of 5-HT synapses in a network model (see Methods). Our model consisted of 5000 conductance-based leaky-integrate-and-fire 5-HT neurons, building on recent simplified single-cell modeling of 5-HT neurons (Harkin et al., 2021). 25% of 5-HT neurons received excitatory input from LHb

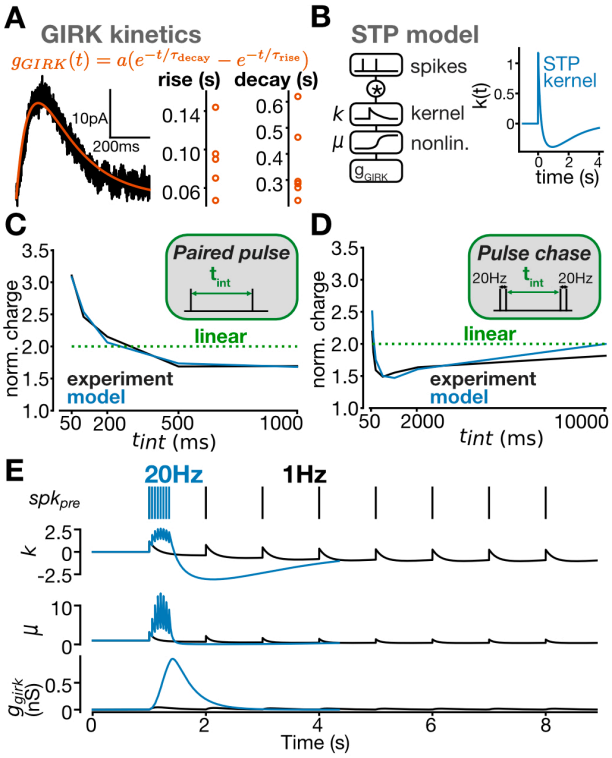

Figure 4: A quantitative model of short-term release dynamics captures patterned inputs. **(A)** Representative trace of kinetics fitted to an averaged electrically evoked GIRK current, and parameter distribution across the population (n=6 neurons). **(B)** Schematic depicting the linear-nonlinear short-term plasticity model and the plasticity kernel fitted using a least-squares approach to paired-pulse data. **(C)** Post-stimulus charge as a function of paired-pulse time interval, depicting experimental mean (black) and model predictions with fitted kernel and nonlinearity (blue). **(D)** Post-stimulus charge as a function of pulse-chase time interval, depicting experimental mean (black) and model predictions (blue). Note that model was fitted to paired-pulse, not pulse-chase dataset. **(E)** Simulations showing responses to 1Hz (black) and 20Hz (blue) presynaptic input, the model variables, and the resulting GIRK conductance.

($\Sigma 7.5\ nS$), while all 5-HT neurons received background Poisson excitation as well as 5-HT$_{1A}$R-mediated inhibition from other 5-HT neurons ($\Sigma 2.5 nS$) (Fig. 5A). The 5-HT synapse of recurrent inhibitory network were imparted with both the experimentally-fitted event kinetics and the short-term dynamics described above (*i.e.,* from the SRP model).

To better understand how 5-HT neuron activity responded to LHb, we considered a range of LHb input frequencies and tracked 5-HT output over multiple timescales (Fig. 5). Responses to sustained 5 Hz or 20 Hz LHb activity suggested three periods (Fig. 5B-C): 1) an early phasic period (0-200 ms) followed by 2) a relaxation to a steady-state response (200-400 ms), and finally 3) a post-stimulus period. The early period resulted from 5-HT neurons responding to direct LHb excitation before 5-HT$_{1A}$R -mediated feedback inhibition could modulate the response. Consequently, the early period output rate was a rectified linear function of the input frequency (Fig. 5D). In contrast, the steady-state response was non-monotonic, displaying an inverted-U shape which peaked at input frequencies around 5 Hz and progressively decreased with higher LHb input frequencies (Fig. 5E). This atypical non-monotonic shape, essentially representing excitation-driven net inhibition, depended on the potent short-term facilitation at 5-HT synapses, as *in silico* removal of these short-term dynamics (while preserving the recurrent architecture) recovered a linear, monotonic, input-output function (Fig. 5E). In contrast, the early or post-stimulus period were not qualitatively affected by the removal of short-term recurrent dynamics (Fig. 5D-F). We repeated these simulations with connection probability decreased tenfold, which revealed qualitatively similar results, supporting the contention that these results may persist over a wide variety of possible network architectures (Fig S8). This indicated that the specific short-term dynamics, not the network architecture itself, was responsible for shaping excitation and inhibition. Together, these results suggests that synaptic dynamics imbue the serotonergic recurrent network with non-monotonic responses to long-range inputs, where response polarity is inverted at high input frequencies.

Recent work has indicated that there are multiple, largely non-overlapping submodules or cellular subgroups within DRN with distinct connectivity and functional rules (Ren et al., 2018; Huang et al., 2019; Paquelet et al., 2022), leading us to ask whether recurrent connections and their particular dynamics could gate interaction between functionally separate submodules or cellular assemblies. We modelled the canonical scenario of reward anticipation, where 5-HT neurons have been shown to display a ramping up of their activity from the time of cue to reward delivery (Zhong et al., 2017). We considered a simplified but realistic (based on Ren et al., 2018) model with two functionally distinct DRN submodules, one receiving step inputs from LHb, the other receiving ramping inputs from another generic area termed A (Fig. 6A). We first asked whether LHb inputs delivered to one submodule could modulate responses of the second, anatomically distinct submodule driven by area A. Ramping input from area A produced a corresponding activity ramp in A-recipient 5-HT neurons, qualitatively matching the 5-HT population responses observed *in vivo* during reward anticipation (Zhong et al., 2017). This population response was minimally influenced by low-frequency LHb inputs (Fig. 6B-C, left), yet high-intensity LHb drive (20 Hz) sharply disrupted A-driven 5-HT activity ramps (Fig. 6C-D, right) despite these LHb inputs not directly contacting A-recipient 5-HT neurons. To further characterize the interaction between 5-HT submodules, we computed the A-driven input-output transformation. The gain of this transformation was not altered by low-frequency LHb input (5 Hz), but was strongly depressed by high-frequency LHb input (Fig. 6D). Thus, strong LHb inputs to DRN have the ability to suppress anatomically separate submodules through recurrent inhibition, implementing a winner-take-all computation. Furthermore, additional simulations

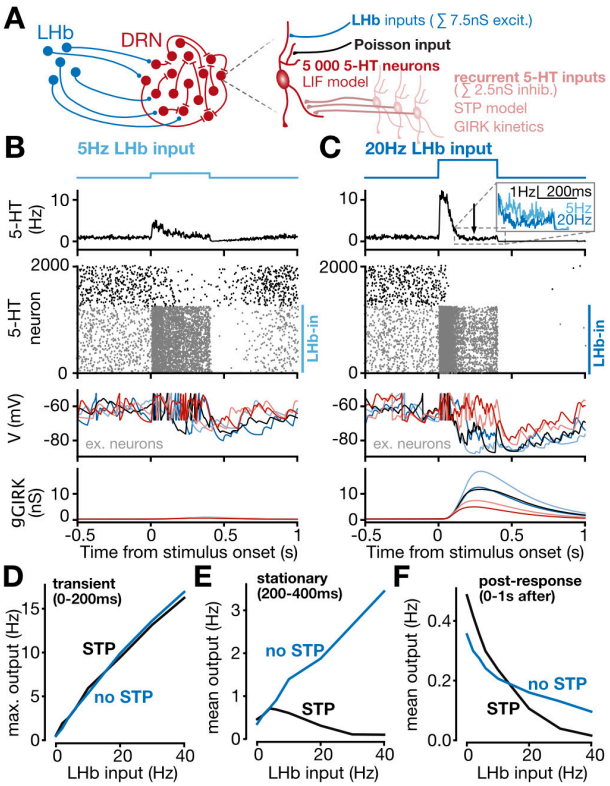

Figure 5: Habenula input to raphe generates a nonmonotonic network response through recurrent short-term plasticity. **(A)** Schematic of the LIF network model. **(B)** Results of a simulation where a 5Hz step input from LHb was delivered to a subset of 5-HT neurons. **(C)** Results of a simulation where a 20Hz step input from LHb was delivered to a subset of 5-HT neurons. **(D)** Input-output transformation for the transient (0-200ms) response phase, with (black) and without (blue) STP rules at recurrent serotonergic connections. **(E)** Input-output transformation for the stationary (200-400ms) response phase, with (black) and without (blue) STP rules at recurrent serotonergic connections. **(F)** Input-output transformation for the post-response (0-1s after stimulus) phase, with (black) and without (blue) STP rules at recurrent serotonergic connections.

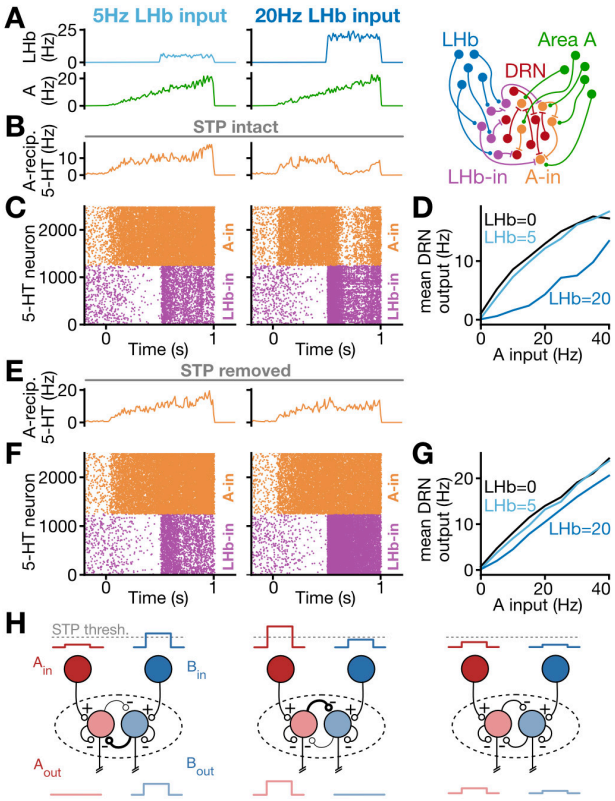

Figure 6: Winner-take-all dynamics generated by recurrent short-term plasticity. **(A)** Simulations with LHb inputs of either 5Hz (left) and 20Hz (middle) were delivered to 5-HT neurons during ramp input from area A. Schematic of LIF network model with two inputs (right). **(B)** Mean responses of 5-HT neurons to 5Hz (left) and 20Hz (right) input with STP rules intact. **(C)** Raster plot showing 5-HT neuron responses to 5Hz (left) and 20Hz (right) input with STP rules intact. **(D)** Input-output function, for input A, with STP rules intact and coincident LHb input at 0, 5 or 20Hz. **(E)** Mean responses of 5-HT neurons to 5Hz (left) and 20Hz (right) input with STP rules removed. **(F)** Raster plot showing 5-HT neuron responses to 5Hz (left) and 20Hz (right) input with STP rules removed. **(G)** Input-output function, for input A, with STP rules removed and coincident LHb input at 0, 5 or 20Hz. **(H)** Schematic of winner-take-all computation with recurrently connected submodules. When one input crosses an STP threshold, output from that submodule dominates while other submodules are suppressed through recurrent inhibition (left and centre). When neither input crosses an STP threshold, outputs from both submodules persist (right).

where we decreased the recurrent connection probability tenfold yielded qualitatively similar results (Fig. S9), indicating that these processing rules were not confined to narrow implementation of different network connectivity features.

To determine whether the short-term plasticity rules were necessary for the nonlinear computations, we performed additional simulations with *in silico* removal of the short-term dynamics (*i.e.,* with linearly summating 5-HT synapses) while preserving recurrent architecture. These simulations revealed that without the STP dynamics, A-driven 5-HT ramps were largely unaffected by either weak or strong LHb input (Fig. 6E-F). Furthermore, without STP, the gain of the A-driven input-output transformation was not significantly modulated by LHb input strength (Fig. 6G). Together, these results indicate that the short-term dynamics of the recurrent 5-HT synapses are necessary to generate winner-take-all computations (Fig. 6H) where strong inputs (*e.g.* acute threat information from LHb) can inhibit weaker input-driven responses to dominate network output.

We next tested the biological plausibility of these winner-take-all rules through additional slice physiology experiments, where either habenula input or local recurrent connections were optogenetically stimulated to gate spiking output. First, a sparse ChETA expression paradigm was employed in DRN as described earlier (Fig. 2; Fig. 7A). In ChETA-negative 5-HT neurons, optical stimulation elicited outward 5-HT_{1A}R currents (Fig. 7B). To directly test whether recurrent connections could gate spiking output of (ChETA-negative) 5-HT neurons, we examined the ability of high-frequency (20 Hz) optical stimulation of DRN ChETA-expressing neurons to perturb the persistent spiking induced by direct current injection of 5-HT neurons (Fig. 7C-7D). Consistent with predictions from our computational model, photostimulation triggered a significant reduction in spiking (Fig. 7D-E) which was mediated by 5-HT_{1A}Rs (Fig. 7F-L). These data indicate that within DRN, recurrent inhibition can allow populations of 5-HT neurons to significantly shape spiking output of separate 5-HT populations. To ensure that the plausibility of these results extend to activation of long-range synaptic input, we found that high-frequency optical stimulation of LHb afferents in slice reliably inhibited spiking output of 5-HT neurons through 5-HT1ARs (Fig. S10).

Together, these findings indicate that the unique short-term dynamics present at DRN 5-HT synapses can facilitate key emergent network computations, including an input frequency-dependent polarity switch leading to network shutdown at high input rates, and winner-take-all dynamics where recurrent inhibition strongly suppresses submodules with weaker inputs.

Learned cue-reward associations are conditionally modulated by habenular drive to the DRN.

A synthesis of these local computations enacted by the DRN recurrent inhibitory motif makes circumscribed predictions about how the statistics of synaptic inputs to DRN should modulate 5-HT output and, by extension, DRN-dependent behaviors. Our ethological inspiration comes from recent work demonstrating that dynamics of DRN and LHb can represent behavioral state transitions (Marques et al., 2020; Amo et al., 2014; Lecca et al., 2020). Moreover, cue-reward learning has been shown to lead to a gradual increase in the population activity of 5-HT neurons during reward anticipation, peaking around reward delivery (Zhong et al., 2017). Because the internal state of reward anticipation can lead to measurable motor outputs such as post-cue anticipatory licking whose dynamics are modulated by 5-HT activity (Matias et al., 2017), we set out to develop a head-fixed classical conditioning task where we could optogenetically manipulate LHb inputs to DRN while monitoring licking behaviors as a metric of reward anticipation-linked internal state.

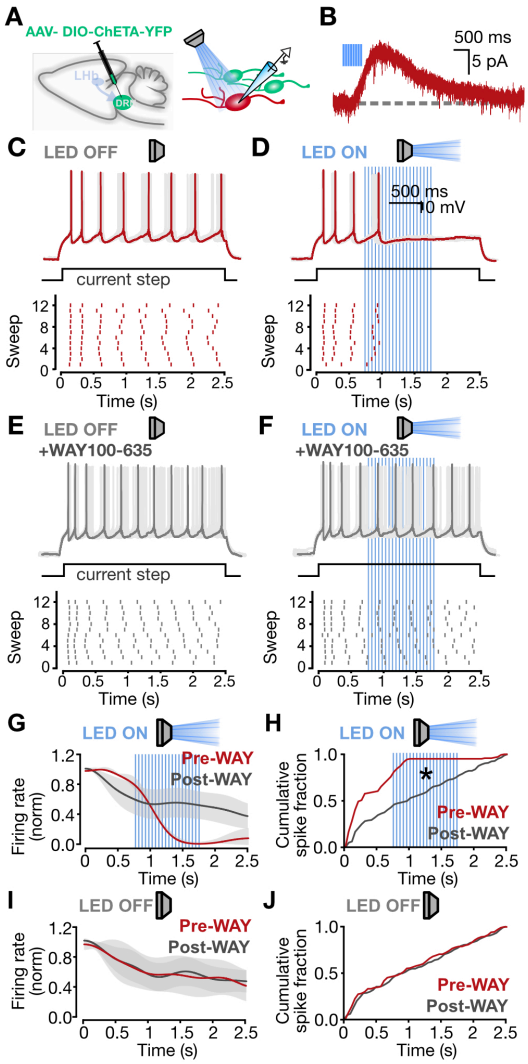

Figure 7: Recurrent inhibition gates spiking activity of 5-HT neurons. **(A)** Schematic of experimental design. Left, AAV-DIO-ChETA-YFP is injected into the DRN at a 2:1 ratio with Mannitol. Right, whole-cell recordings from ChETA-negative 5-HT neurons. **(B)** Recurrent 5HT1AR-mediated current in ChETA-negative 5-HT neuron. **(C)** Spiking of a 5-HT neuron in response to current injection. Below, raster plot showing the same neuron's activity across trials. **(D)** Spiking of a 5-HT neuron in response to current injection and 20Hz optical activation of CHETA-positive 5-HT neurons. Below, raster plot showing the same neuron's activity across trials.**(E)** Spiking of a 5-HT neuron in response to current injection in the presence of WAY100-635. Below, raster plot showing the same neuron's activity across trials. **(F)** Spiking of a 5-HT neuron in response to current injection and 20Hz optical activation of CHETA-positive 5-HT neurons, in the presence of WAY100-635. Below, raster plot showing the same neuron's activity across trials. **(G)** Smoothed firing rate (normalized) over time for pre- and post-WAY recordings with LED stimulation (mean +- SE, n=3 neurons). **(H)** Cumulative spike fraction in pre- and post-WAY recordings with LED stimulation (n=3 neurons, 2-sample Kolmogorov-Smirnov test: p = 7.4e-15). **(I)** Smoothed firing rate (normalized) over time for pre- and post-WAY recordings without LED stimulation (mean +- SE, n=3 neurons). **(J)** Cumulative spike fraction in pre- and post-WAY recordings with LED stimulation (3 neurons, 2-sample Kolmogorov-Smirnov test: p = 0.85).

Our experimental and modeling work so far predicts that the statistics of incoming habenula input should determine whether DRN 5-HT neurons are excited or inhibited over protracted timescales: low-frequency LHb inputs to DRN should promote reward anticipation-linked activity ramps, while high-frequency LHb (*e.g.* severe threats), should suppress this activity by recruiting strong short-term facilitation of recurrent inhibition within DRN. Mice received a bilateral injection of AAV-ChR2-mCherry in LHb while an optic fiber was implanted in DRN and a custom 3D-printed head bar affixed to the skull (Fig. 8A; see Methods). Mice underwent water deprivation before being trained on an auditory classical conditioning paradigm where one of three auditory cues (discriminable single frequency tones; de Hoz & Nelken, 2014) was randomly presented for each trial, followed by delayed delivery of either a small (5uL), a large reward (10uL), or no reward (Fig. 8B). Trained mice displayed robust cue-driven anticipatory licking, a conditioned response which indicates expression of a learned stimulus-reward association (Cohen et al., 2012). This conditioned licking response was strongest after large reward cues (Fig. 8C, left), and we also observed robust reward-driven licking (Fig. 8C, right). Animals were considered trained if they reached a criterion performance of anticipatory licking during large reward trials (see Methods).

To assess the behavioral impact of optogenetically activating the habenula input to the raphe, we devised a trial structure interleaving optogenetically stimulated and non-stimulated trials to permit within-animal behavioral comparisons for each discrete reward value (Fig. 8D, top). During stimulated trials, LHb afferents in the DRN were optogenetically activated by brief pulses of blue light during the period between cue and reward presentation (see Methods). During non-stimulated large reward trials, animals displayed robust conditioned anticipatory licking after the auditory cue (Fig. 8E, black). High frequency (20Hz) photostimulation of LHb afferents induced a striking and rapid decrease in anticipatory licking which recovered rapidly after stimulation ceased (Fig. 8E, blue). In contrast, in agreement with our quantitative model predictions, low-frequency 5 Hz optogenetic stimulation had no effect on conditioned anticipatory licking (Fig. 8F). Anticipatory behavior was quantified by calculating the difference in mean cue-driven anticipatory licking between non-stimulated and interleaved stimulated trials for each animal; this analysis revealed a significant group difference between 20 Hz and 5 Hz stimulation on acute reward anticipation for large-reward trials (Fig. 8G).

As current theories postulate that 5-HT neurons represent valence information during associative learning (Liu et al., 2017), we next focused on the effect of photostimulation during small reward and no reward trials. We hypothesized that since these trials had lower expected reward values, activating LHb inputs to DRN would have a lesser impact on reward anticipation compared to large reward trial stimulation. During small reward trials, neither 20Hz or 5Hz photostimulation modulated anticipatory licking (Fig. 8J; Fig. S11B-C) despite the fact that mice showed anticipatory licking during interleaved non-photostimulated trials (Fig. S11B-C; Fig. 8C). For trials where no reward was delivered, photostimulating at 5Hz after the auditory tone triggered a slight, but at times clearly noticeable, increase in licking which was not seen during 20Hz photostimulation (Fig. 8K; Fig. S11D-E). These contextual effects on reward anticipation, whose sign and magnitude depend on both reward value and LHb input statistics, are broadly consistent with a model where recurrent inhibition leads to antagonistic competition between distinct valence representations spanning multiple timescales and submodules in DRN (Cohen et al., 2015; Ren et al., 2018).

To control for visual artifacts, we stimulated at 20 Hz with yellow light, which is beyond the excitation spectrum of ChR2 (Miyazaki et al., 2018; see Methods) and found no visual cue-

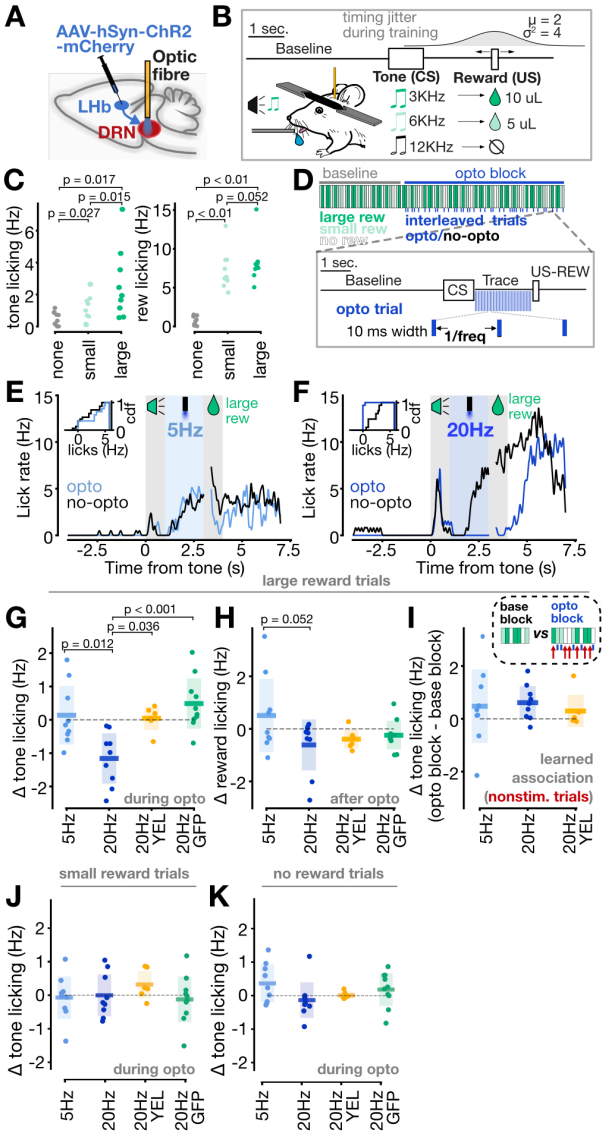

Figure 8: Habenula input to raphe disrupts the expression of learned reward associations in a value- and frequency-dependent manner. **(A)** Schematic illustrating experimental setup (left) and confocal image of LHb injection site (right). **(B)** Schematic of head-fixed classical conditioning task. **(C)** Mice learned to lick in response to the small reward-predicting and large reward-predicting cues (left), and displayed elevated licking after reward delivery (right) (n=9 mice). **(D)** Schematic of trial structure for optogenetic manipulations. **(E)** Mean licking across all large reward trials for a single mouse depicting control trials (black) or 5Hz optogenetic stimulation trials (blue). Inset shows cumulative distribution of licking for all large-reward trials. **(F)** Mean licking across all large reward trials for a single mouse depicting control trials (black) or 20Hz optogenetic stimulation trials (blue). Inset shows cumulative distribution of licking for all large-reward trials. **(G-I)** Summary statistics for optogenetic manipulation during post-tone period of large-reward trials. **(G)** Change in conditioned licking response during tone presentation, between control and optogenetic stimulation trials during opto block (paired two-sided t-tests). **(H)** Mean reward licking change between control and optogenetic stimulation trials (paired two-sided t-tests). **(I)** Change in post-tone licking for nonstimulated trials between baseline block and optogenetic stimulation block. **(J)** Change in post-tone licking between control and optogenetic stimulation trials (small reward trials). **(K)** Change in post-tone licking between control and optogenetic stimulation trials (no reward trials).

induced effect on conditioned licking (Fig. 8G; yellow). As a separate control, in another cohort where AAV-GFP was injected bilaterally in LHb and an optic fiber implanted in DRN, 20 Hz stimulation with blue light did not elicit changes in conditioned licking (Fig. 8G, green). Finally, to rule out nonspecific stimulation-induced motor effects, we additionally photostimulated at high frequencies during the reward consumption phase and observed no significant modulation of licking in these conditions (Fig. S11F-G).

It is possible that the LHb inputs to the DRN may affect expression of conditioned responses or reward consumption over longer timescales, either within the same trial or across trials, possibly reflecting changes in cognitive flexibility or learning (Matias et al., 2017; Zhong et al., 2017). We assessed this in two ways. First, we examined licking behavior after acute stimulation had ended (*i.e.,* during reward delivery) and compared stimulated and non-stimulated trials. 20Hz stimulation slightly but nonsignificantly reduced licking during reward consumption compared to 5Hz stimulation, likely reflecting a seconds-long persistent effect of stimulation consistent with the timescale of GIRK activation (Fig. 8H). Second, we considered whether LHb activation updated the underlying cue-reward association within the session, which would manifest as changes in anticipation during interleaved, nonstimulated trials. We calculated the difference in conditioned licking response between the baseline block (first 40 trials) and nonstimulated trials during the opto block (last 80 trials), revealing no long-term changes in reward anticipation (Fig. 8I). From this, we conclude that at high input frequencies, the LHb input to the raphe acutely modulates behavior over timescales of hundreds of milliseconds, consistent with the timescales of GIRK inhibition uncovered in slice, yet does not modulate the conditioned association itself.

We additionally considered how behavioral variability between animals correlated with the effects of stimulation. We found that animals with more anticipatory licking experienced slightly greater suppression of licking upon high frequency stimulation (Fig. S11H). However, at low stimulation frequencies, there was a slight positive relationship between anticipation and stimulation effects (Fig. S11H). Finally, we observed no correlation between effects of high and low stimulation frequency across animals (Fig. S11I).

Together, these results indicate that LHb input to DRN suppresses reward anticipation in a frequency-dependent and temporally precise manner, exclusively during high reward value states. At high input frequencies, where strong STP-dependent recurrent inhibition is expected to dominate, anticipatory licking was suppressed; yet, at lower input frequencies where network excitation dominates, anticipatory licking was either not altered, or even enhanced slightly. During low reward value states, LHb input does not appear to substantively modulate reward anticipation. These behavioral results highlight how habenula inputs to raphe can alter behavioral state dynamics over protracted timescales in a manner contingent on input statistics and short-term recurrent dynamics.

Discussion

Here, using a combination of optogenetic, electrophysiological, computational and behavioral approaches, we provide evidence that DRN is organized in an unsuspected recurrent inhibitory network, characterized by strong short-term release dynamics active over protracted timescales. We outline a core set of computations supported by this connectivity motif when activated by long-range excitatory LHb input, including a reversal of network response polarity at high input frequencies, and a winner-take-all computation where anatomically independent raphe subsystems can be antagonistically coupled via recurrent inhibition. Building on key

predictions from this network modeling, we found behavioral manifestations of this non-linear network computation of the DRN in a frequency-dependent inhibition of reward anticipation triggered by LHb inputs to the DRN. These results add to the reported role of 5-HT in modulating cognitive processing, not direct appetitive or aversive proximal behaviors (Fonseca et al., 2015; Miyazaki et al., 2018) and links a local circuit's network architecture, and associated synaptic dynamics, to a core set of ethologically relevant computations.

We present several lines of experimental evidence supporting a connectivity model whereby 5-HT neurons in the DRN are organized in a local recurrent inhibitory network, including the observation that photostimulation of a subset of opsin-expressing 5-HT neurons induced robust 5-HT_{1A}R -mediated hyperpolarization/outward currents in in non-opsin-expressing 5-HT neurons postsynaptic to the stimulated ensemble. This experimental architecture represents in effect an optogenetic equivalent of paired recordings from synaptically-connected neurons, which have provided decisive functional validation of the recurrent connectivity nature of several networks in the brain (Miles & Wong, 1986; Mason et al., 1991; Markram et al., 1997; Debanne et al., 2008). These experiments, unambiguously showing functional connections between 5-HT neurons, supports a model which is largely inconsistent with the widely and long-held idea that 5-HT neurons are regulated in an autocrine fashion by dendritically-released 5-HT acting on so-called 5-HT_{1A}R somatodendritic autoreceptors (Gozlan et al., 1983; Weissmann-Nanopoulos et al., 1985; Pineyro & Blier, 1999). This autoreceptor hypothesis makes several experimental predictions which we directly tested and failed to find support for. While our results do not formally allow to distinguish whether interconnected 5-HT neurons communicate through dendro-dendritic or canonical axo-dendritic functional contacts, or whether release of 5-HT is spatially confined or consists of more spatially diffuse volume transmission (Maxwell et al., 1983; Ridet et al., 1994; Bunin & Wightmann, 1998), we nonetheless note that classic axonal release provides the most parsimonious and credible model accounting for our results. While a subset of 5-HT dendrites contains 5-HT containing vesicles (Descarries et al., 1982; Chazal and Ralston, 1987), 5-HT containing axon terminals are nonetheless widespread in the DRN and are structurally indistinguishable from those found elsewhere in the brain (Chazal and Ralston, 1987). Importantly, this view does not preclude the presence of NMDAR-dependent dendritic release of 5-HT that may operate in distinct physiological conditions (Colgan et al., 2012).

While there is compelling evidence that 5-HT is packaged in, and released from, vesicles (De-Miguel & Trueta, 1995), and mechanisms of 5-HT release in DRN have begun to be investigated (Courtney & Ford, 2016), an algorithmic description of its release dynamics over multiple timescales, and their underlying computations has been lacking. Through a series of minimal electrical stimulation experiments, we obtained strong evidence that 5-HT is released probabilistically, with complex facilitation and depression dynamics which could be precisely captured by a kernel-based synaptic release model. Previous work, relying on bulk monitoring of 5-HT release by fast-scan cyclic voltammetry, in contrast showed quasi-deterministic release of 5-HT and minimal short-term dynamics (Bunin & Wightman, 1998). Our approach rather relied on the non-desensitizing 5-HT_{1A}R-activated GIRK conductance as a reporter of 5-HT release (Fig. S6), and a statistical analysis of these events showed effective stimulation of a few 5-HT synapses (perhaps as little as one) was consistent with probabilistic release of 5-HT. It is likely that the distinct granularity of this approach compared to that afforded by voltammetry underlies some of these discrepancies. Irrespective of this point, it is still intriguing to emphasize that the nature of the short-term dynamics of 5-HT release stands in stark contrast to the robustly

depressing dopamine release dynamics recently described in striatum (Liu et al., 2018, Liu et al., 2021). Especially considering that several features of neurotransmitter release are dictated by the postsynaptic target cell type (Geddes et al., 2016; Koester & Johnston, 2005; Campagnola et al., 2022), future work will be required to determine whether the short-term synaptic dynamics reported here in the DRN are shared by other 5-HT synapses in the brain. These points of discussion nonetheless collectively point to our still rudimentary understanding of monoaminergic transmission dynamics and their underlying computations, especially when compared to those described for fast neurotransmitter release (Abbott & Regehr, 2004; Jackman & Regehr, 2017).

Through a series of constrained network models, we inferred several computations supported by the inhibitory recurrent network in DRN. Previous experimental and theoretical work has identified a number of possible computational functions of network recurrence, including winner-take-all competition (Coultrip et al., 1992), signal amplification and selectivity (Douglas et al., 1995) and probabilistic inference (Echeveste et al., 2020); however, the potential computations performed by recurrent *inhibition* over timescales of seconds were not immediately obvious. While canonical winner-take-all implementations require simple feedback inhibition from a shared interneuron (Coultrip et al., 1992), the implementation in DRN has several unique features. The extended timescale of the inhibitory GIRK conductance, lasting seconds, adds a history component to the winner-take-all computation. Additionally, the strong facilitation at recurrent inhibitory synapses amplifies inherent winner-take-all dynamics: past some facilitation threshold, as strongly activated groups of neurons inhibit less activated groups, they additionally receive less recurrent inhibition from these groups (Fig. 6H). Our model is experimentally grounded in several fundamental ways. First, individual 5-HT neurons were modeled with parameters extracted from an established integrate-and-fire framework (Harkin et al., 2021, Pozzorini et al., 2015). Second, the short-term dynamics at recurrent connections were modeled using a linear-nonlinear formalism (Rossbroich et al., 2021) which precisely captured responses to a test set of patterned input. Third, the core network computations persisted over a wide range of possible recurrent connectivity schemes, while *in silico* removal of the short-term recurrent dynamics themselves disrupted these computations. Finally, we tested key physiological predictions of a winner-take-all network, including that serotonergic spiking can be suppressed by activation of recurrently connected neurons. By developing a formalism linking synaptic dynamics with emergent computations, we have provided a flexible architecture for understanding how local serotonergic circuitry is modulated by long-range inputs.

Our results show that the recurrent inhibitory dynamics lead to a non-monotonic input-output relationship in the DRN by supporting a strong excitation-driven inhibition, where larger excitatory inputs generate greater network suppression. A natural question is how this computation compares with gain control associated with classical feedforward inhibition motif. A range of distinct gain control regimes have been described with feedforward inhibition such as subtractive and divisive inhibition (Ayaz & Chance, 2009) and even non-monotonic inhibition (Mejias et al., 2014; Lewis et al., 2007). However, the recurrent inhibition motif described here is unique in that the phasic network response is dominated by direct excitation and linearly reports input intensity, while the delayed steady-state response exhibits non-monotonic behavior with increasing excitation. In principle, these temporally distinguishable epochs of 5-HT output dynamics could support multiplexed codes such as valence encoding over multiple timescales (Cohen et al., 2015). Our network model additionally uncovered an emergent winner-take-all-like computation in the DRN, where strong activation of connected modules of 5-HT neurons

can inhibit activity of others. This builds on previous work describing anatomically segregated DRN subdomains (Ren et al., 2018), and implies that a winner-take-all computation governs behavioral state selection between submodules. While these simulations uncovered general algorithmic principles which were tested with a range of connectivity profiles in our network models, more precise quantitative information on the recurrent connectivity between submodules (Ren et al., 2018) or on the additional recruitment of feedforward GABAergic inhibition by some inputs (Zhou et al., 2017; Geddes et al., 2016) should bring about refinement of these general principles.

By combining patterned *in vivo* optogenetic stimulation of LHb inputs to the DRN with an auditory classical conditioning task, we were able to test key predictions from our network modeling, and found that high-frequency, but not low-frequency, activation suppressed anticipatory licking before large rewards. While we optically stimulated LHb inputs in the DRN at 5Hz and 20Hz, these frequencies do not represent a one-to-one mapping onto habenular firing rates observed *in vivo*, since release probability is artificially inflated during optogenetic stimulation, and real population firing rates are likely highly heterogeneous and asynchronous over time. Thus, these frequencies are likely underestimates of the dynamic range of LHb firing rates within which the frequency-dependent inversion in the DRN occurs *in situ*. Nonetheless, a key finding of these experiments is that the behavioral effect of high-frequency activation was temporally precise, lasting several hundred milliseconds (in line with the timescale of a 5-HT_{1A}R-mediated GIRK activation) and did not extend beyond the running trial. Furthermore, the effect of optogenetic stimulation was specific to the anticipatory licking period, and did not reflect a non-specific, general inhibitory role on motor output since it was ineffective when administered during reward consumption. As a whole, these findings are consistent with previous work showing that optogenetically activating DRN promotes waiting, but is not rewarding and does not directly drive motor actions in and of itself (Fonseca et al., 2015; Miyazaki et al., 2018). More broadly, our behavioral results provide evidence that LHb inputs to the DRN rapidly and reversibly alter behavioral state, which is consistent with previous findings on the habenulo-raphe pathway (Amo et al., 2014; Marquez et al., 2020) and may represent an important role for this pathway in dynamic state selection.

Animals often exhibit sharp thresholds when transitioning between ethologically relevant behavioral states such as exploitation and exploration (Marques et al., 2020). These state transitions require brain circuits which continually evaluate graded representations of either internal or external cues, enacting thresholding operations on behavioral timescales. For example, threat may be best conjectured as being cautiously invigorating when small (go), but nefarious when strong (no-go). Building on recent theories (Liu et al., 2020; Luo et al., 2016; Cohen et al., 2015; Marques et al., 2020), the winner-take-all computation between ensembles of recurrently connected 5-HT neurons, operating over protracted timescales, satisfies many of the conditions required for the largely exclusive, non-overlapping implementation of distinct naturalistic behaviors (Ren et al., 2018).

Acknowledgements

This work was supported by grants from the Canadian Institute for Health Research (JCB; RN), the uOttawa Brain and Mind Institute and the Canadian Heart and Stroke Foundation (JCB), Brain Canada (JCB), and the Canadian Foundation for Innovation (JCB). We thank members of the Beique, Naud and Maler lab for helpful discussions. We would also like to thank Drs Salah El Mestikawy and Sylvain Williams for providing us with the SERT-CRE mouse line.

Author contributions

Conceptualization, M.B.L., S.G., S.H-D., R.N., and J.-C.B.; Methodology, M.B.L., S.G. ; Software, M.B.L.; Formal Analysis, M.B.L.; Investigation, M.B.L., S.G., M.C., E.H., S.M., E.H.-G., ; Resources, M.B.L., E.H. and R.N. ; Writing – Original Draft, M.B.L., S.G.; Writing – Review & Editing, M.B.L., R.N., and J.-C.B.; Supervision, J.-C.B.; Funding Acquisition, J.-C.B.

Declaration of interests

The authors declare no competing interests.

Data Availability

The datasets generated during the current study are available from the corresponding author on reasonable request.

Code Availability

The code generated during the current study are available from the corresponding author on reasonable request.

References

Abbot, L.F. & Regehr, W.G. (2004). Synaptic computation. Nature 431:796-803.

Amo, R., Fredes, F., Kinoshita, M., Aoki, R., Aizawa, H., Agetsuma, M., Aoki, T., Shiraki, T., Kakinuma, H., Matsuda, M., Yamazaki, M., Takahoko, M., Tsuboi, T., Higashijima, S.-I., Miyasaka, N., Koide, T., Yabuki, Y., Yoshihara, Y., Fukai, T. & Okamoto, H. (2014) The habenulo-raphe serotonergic circuit encodes an aversive expectation value essential for adaptive active avoidance of danger. Neuron 84:1034-1048.

Andrade, R., Malenka, R.C. & Nicoll, R.A. (1986). A G protein couples 5-HT and GABAB receptors to the same channels in hippocampus. Science 234:1261-1265.

Ayaz, A. & Chance, F.S. (2009). Gain modulation of neuronal responses by subtractive and divisive mechanisms of inhibition. J Physiol 101:958-968.

Broadhurst, P.L. (1957). Emotionality and the Yerkes-Dodson Law. J Exp Psychol 54:345-352.

Bromberg-Martin, E.S. & Hikosaka, O. (2011). Lateral habenula neurons signal errors in the prediction of reward information. Nat Neurosci 14:1209-1216.

Bunin, M.A. & Wightman, R.M. (1998). Quantitative evaluation of 5-hydroxytryptamine (5-HT) neuronal release and reuptake: an investigation of extrasynaptic transmission. J Neurosci 18:4854-4860.

Campagnola, L., Seeman, S.C., Chartrand, T., Kim, L., Hoggarth, A., Gamlin, C., Ito, S., Trinh, J., Davoudian, P., Radaelli, C., et al., (2022). Local connectivity and synaptic dynamics in mouse and human neocortex. Science 375: eabj5861. DOI: 10.1126/science.abj5861.

Celada, P., Puig, V.M., Casanovas, J.M., Guillazo, G. & Artigas, F. (2001). Control of dorsal raphe serotonergic neurons by the medial prefrontal cortex: Involvement of serotonin-1A, GABAA, and glutamate receptors. J Neurosci 21:9917-9929.

Chazal, G. & Ralston, H.J. (1987). Serotonin-containing structures in the nucleus raphe dorsalis of the cat: An ultrastructural analysis of dendrites, presynaptic dendrites, and axon terminals. J Comp Neurol 259:317-329.

Cohen, J.Y., Amoroso, M.W. & Uchida, N. (2015). Serotonergic neurons signal reward and punishment on multiple timescales. eLife 2015;4:e06346.

Cohen, J.Y., Haesler, S., Vong, L., Lowell, B.B. & Uchida, N. (2012). Neuron-type-specific signals for reward and punishment in the ventral tegmental area. Nature 482:85-88.

Coffey, K.R., Marx, R.G., Vo, E.K., Nair, S.G. & Neumaier, J.F. (2020). Chemogenetic inhibition of lateral habenula projections to the dorsal raphe nucleus reduces passive coping and perseverative reward seeking in rats. Neuropsychopharm 45:1115-1124.

Colgan, L.A., Cavolo, S.L., Commons, K.G. & Levitan, E.S. (2012). Action potential-independent and pharmacologically unique vesicular serotonin release from dendrites. J Neurosci 32:15737-15746.

Coultrip, R., Granger, R. & Lynch, G. (1992). A cortical model of winner-take-all competition via lateral inhibition. Neural Networks 5:47-54.

Courtney, N.A. & Ford, C.P. (2016). Mechanisms of 5-HT_{1A} receptor-mediated transmission in dorsal raphe 5-HT neurons. J Physiol 594:953-965.

Cragg, S. (2003). Variable dopamine release probability and short-term plasticity between functional domains of the primate striatum. J Neurosci 23:4378-4385.

Debanne, D., Boudkkaszi, S., Campanac, E., Cudmore, R.H., Giraud, P., Fronzaroli-Molinieres, L., Carlier, E. & Caillard, O. (2008). Paired-recordings from synaptically coupled cortical and hippocampal neurons in acute and cultured brain slices. Nat Protocols 3:1559-1568.

de Hoz, L. & Nelken, I. (2014). Frequency tuning in the behaving mouse: Different bandwidths for discrimination and generalization. PLOS One 9:e91676.

Denève. S. & Machens, C.K. (2016). Efficient codes and balanced networks. Nat Neurosci 19:375-382.

Descarries, L., Watkins, K.C., Garcia, S. & Beaudet, A. (1982). The serotonin neurons in nucleus raphe dorsalis of adult rat: A light and electron microscope radioautographic study. J Comp Neurol 207:239-254.

Dolzani, S.D., Baratta, M.V., Amat, J., Agster, K.L., Saddoris, M.P., Watkins, L.R. & Maier, S.F. (2016). Activation of a habenulo-raphe circuit is critical for the behavioral and neurochemical consequences of uncontrollable stress in the male rat. eNeuro 3:e0229-16.2016.

Dorocic, I.P., Futh, D., Xuan, Y., Johansson, Y., Pozzi, L., Silberberg, G., Carlen, M. & Meletis, K. (2014). A Whole-brain atlas of inputs to serotonergic neurons of the dorsal and median raphe nuclei. Neuron 83:663-678.

Douglas, R.J., Koch, C., Mahowald, M., Martin, K.A.C. & Suarez, H.H. (1995). Recurrent excitation in neocortical circuits. Science 269:981-985.

Echeveste, R., Aitchison, L., Hennequin, G. & Lengyel, M. (2020). Cortical-like dynamics in recurrent circuits optimized for sampling-based probabilistic inference. Nat Neurosci 23:1138-1149.

Eriksson, A., Raczkowska, M., Navawongse, R., Choudhury, R., Stewart, J.C., Tang, Y.L., Wang, Z., Claridge-Chang, A. (2017). Neuromodulatory circuit effects on Drosophila feeding behaviour and metabolism. Sci Rep 7:8839.

Geddes, S.D., Assadzada, S., Lemelin, D., Sokolovski, A., Bergeron, R., Haj-Dahmane, S. & Beique, J.-C. (2016). Target-specific modulation of the descending prefrontal cortex inputs to the dorsal raphe nucleus by cannabinoids. PNAS 113:5429-5434.

Gozlan, H., El Mestikawy, S., Pichat, L., Glowinski, J. & Hamon, M. (1983). Identification of presynaptic 5-HT autoreceptors using a new ligand: 3H-PAT. Nature 305:140-142.

Graeff, F.G., Guimaraes, F.S., de Andrade, T.G.C.S. & Deakin, J.F.W. (1996). Role of 5-HT in Stress, Anxiety and Depression. Pharmacol Biochem Behav 54:129-141.

Grienberger, C., Milstein, A.D., Bittner, K.C., Romani, S. & Magee, J.C. (2017). Inhibitory suppression of heterogeneously tuned excitation enhances spatial coding in CA1 place cells. Nat Neurosci 20:417-426.

Harkin, E.F., Payeur, A., Lynn, M.B., Boucher, J.-F., Caya-Bissonnette, L., Cyr, D., Stewart, C., Longtin, A., Naud, R. & Béïque, J.-C. (2021). Temporal derivative computation in the dorsal raphe network revealed by an experimentally-driven augmented integrate-and-fire modeling framework. Biorxiv https://doi.org/10.1101/2021.06.25.449907.

Huang, K.W., Ochandarena, N.E., Philson, A.C., Hyun, M., Birnbaum, J.E., Cicconet, M. & Sabatini, B.L. (2019). Molecular and anatomical organization of the dorsal raphe nucleus. eLife 8:e46464.

Jackman, S.L. & Regehr, W.G. (2017). The mechanisms and functions of synaptic facilitation. Neuron 94:447-464.

Jones, E., Oliphant, E., Peterson, P., et al. (2001). SciPy: open source scientific tools for Python. http://www.scipy.org.

Lammel, S., Lim, B.K., Ran, C., Huang, K.W., Betley, M.J., Tye, K.M., Deisseroth, K. & Malenka, R.C. (2012). Input-specific control of reward and aversion in the ventral tegmental area. Nature 491:212-217.

Lecca, S., Namboodiri, V.M.K., Restivo, L., Gervasi, N., Pillola, G., Stuber, G.D. & Mameli, M. (2020). Heterogeneous habenular neuronal ensembles during selection of defensive behaviors. Cell Rep 31:107752.

Lewis, J.E., Lindner, B., Laliberté, B. & Groothius, S. (2007). Control of neuronal firing by dynamic parallel fiber feedback: Implications for electrosensory reafference suppression. J Exp Biol 210:4437-4447.

Li, Y., Zhong, W., Wang, D., Feng, Q., Li, Z., Zhou, J., Jia, C., Hu, F., Zeng, J., Guo, Q., Fu, L. & Luo, Minmin. (2016). 5-HT neurons in the dorsal raphe nucleus encode reward signals. Nat Comms 7:10503.

Liu, C., Goel, P. & Kaeser, P.S. (2021). Spatial and temporal scales of dopamine transmission. Nat Neurosci 22:345-358.

Liu, C., Kershberg, L., Wang, J., Schneeberger, S. & Kaeser, P. (2018). Dopamine secretion is mediated by sparse active zone-like release sites. Cell 172:706-718.

Liu, Z., Lin, R. & Luo, M. (2020). Reward contributions to serotonergic function. Annu Rev Neurosci 43:141-162.

Luo, M., Li, Y. & Zhong, W. (2016). Do dorsal raphe 5-HT neurons encode “beneficialness”? Neurobiol Learn Mem 135:40-49.

Mason, A., Nicoll, A. & Stratford, K. (1991). Synaptic transmission between individual pyramidal neurons of the rat visual cortex *in vitro*. J Neurosci 11:72:84.

Markram, H., Lubke, J., Frotscher, M. & Sakmann, B. Regulation of synaptic efficacy by coincidence of postsynaptic APs and EPSPs. Science 275:213-215.

Marquez, J.C., Li, M., Schaak, D., Robson, D.N. & Li, J.M. (2020). Internal state dynamics shape brainwide activity and foraging behavior. Nature 577:239-243.

Matsumoto, M. & Hikosaka, O. (2009). Representation of negative motivational value in the primate lateral habenula. Nat Neurosci 12:77-84.

Maxwell, D.J., Leranth, C. & Verofstad, A.A.J. (1983). Fine structure of 5-HT-containing axons in the marginal zone of the rat spinal cord. Brain Res 266:253-259.

Mejias, J.F., Payeur, A., Selin, E., Maler, L. & Longtin, A. (2014). Subtractive, divisive and non-monotonic gain control in feedforward nets linearized by noise and delays. Front Comp Neurosci, doi: https://doi.org/10.3389/fncom.2014.00019.

Miles, R. & Wong, R.K.S. (1986). Excitatory synaptic interactions between CA3 neurones in the guinea-pig hippocampus. J Physiol 373:397-418.

Miyazaki, K., Miyazaki, K.W., Sivori, G., Yamanaka, A., Tanaka, K.F. & Doya, K. (2020). Serotonergic projections to the orbitofrontal and medial prefrontal cortices differentially modulate waiting for future rewards. Sci Adv 6:eabc7246.

Miyazaki, K., Miyazaki, K.W., Yamanaka, A., Tokuda, T., Tanaka, K.F. & Doya, K. (2018). Reward probability and timing uncertainty alter the effect of dorsal raphe 5-HT neurons on patience. Nat Comms 9:2048.

Miyazaki, K.W., Miyazaki, K., Tanaka, K.F., Yamanaka, A., Takahashi, A., Tabuchi, S. & Doya, K. (2014). Optogenetic activation of dorsal raphe 5-HT neurons enhances patience for future rewards. Curr Biol 24:2033-2040.

Newberry, N.R. & Nicoll, R.A.A. (1984). A bicuculline-resistant inhibitory post-synaptic potential in rat hippocampal pyramidal cells in vitro. J Physiol 348:239-254.

Paquelet, G.E., Carrion, K., Lacefield, C.O., Zhou, P., Hen, R. & Miller, B.R. (2022). Single-cell activity and network properties of dorsal raphe nucleus serotonin neurons during emotionally salient behaviors. Neuron, doi: 10.1016/j.neuron.2022.05.015.

Pazos, A. & Palacios, J.M. (1985). Quantitative autoradiographic mapping of serotonin receptors in the rat brain. I. Serotonin-1 receptors. Brain Res 346:205-230.

Pineyro, G. & Blier, P. (1999). Autoregulation of 5-HT neurons: role in antidepressant drug action. Pharmacol Rev 51:533-591.

Pozzorini, C., Mensi, S., Hagens, O., Naud, R., Koch, C. & Gerstner, W. (2015). Automated high-throughput characterization of single neurons by means of simplified spiking neurons. PLAS Comp Biol 11:e1004275.

Proulx C.D., Hikosaka, O. & Malinow R. (2014). Reward processing by the lateral habenula in normal and depressive behaviors. Nat Rev Neurosci 17:1146-1152.

Ren, J., Friedmann, D., Xiong, J., Huguenard, J., Horowitz, M.A. & Luo, L. (2018). Anatomically defined and functionally distinct dorsal raphe 5-HT sub-systems. Cell 175:472-487.

Ridet, J.-L., Tamir, H. & Privat, A. (1994). Direct immunocytochemical localization of 5-hydroxytryptamine receptors in the adult rat spinal cord: A light and electron microscopic study using anti-idiotypic antiserum. J Neurosci Res 38:109-121.

Rossbroich, J., Trotter, D., Beninger, J., Toth, K. & Naud, R. (2021). Linear-nonlinear cascades capture synaptic dynamics. PLOS Comp Bio 17(3): e1008013.

Salehi, B., Cordero, M.I. & Sandi, C. (2010). Learning under stress: the inverted-U-shape function revisited. Learn Memory 17:522-530.

Seo, Changwoo., Guru, A., Jin, M., Ito, B., Sleezer, B.J., Ho, Y.-Y., Wang, E., Boada, C., Krupa, N.A., Kullakanda, D.S., Shen, X.C., Warden, M.R. (2019). Intense threat switches dorsal raphe 5-HT neurons to a paradoxical operation mode. Science 363:538-542.

Stephens, D.W. & Krebs, J.R. (1986). Foraging Theory. Princeton: Princeton University Press.

Stimberg, M., Brette, R. & Goodman, D.F.M. (2019). Brian 2, an intuitive and efficient neural simulator. eLife 2019;8:e47314.

Takahashi, A., Lee, R.X., Iwasato, T., Itohara, S., Arima, H., Bettler, B., Miczek, K.A. & Koide, T. (2015). Glutamate input in the dorsal raphe nucleus as a determinant of escalated aggression in male mice. J Neurosci 35:6452-6436.

Trinh, A.-T., Harvey-Girard, E., Teixeira, F. & Maler, L. (2016). Cryptic laminar and columnar organization in the dorsolateral pallium of a weakly electric fish. J Comp Neurol 524:408–428.

Vandermaelen, C.P. & Aghajanian, G.K. (1983). Electrophysiological and pharmacological characterization of serotonergic dorsal raphe neurons recorded extracellularly and intracellularly in rat brain slices. Brain Res 289:109-119.

van der Walt, S., Colbert, S.C., and Varoquaux, G. (2011). The NumPy array: a structure for efficient numerical computation. Comput Sci Eng *13*, 22–30.

Warden, M.R., Selimbeyoglu, A., Mirzabekov, J.J., Lo, M., Thompson, K.R., Kim, S.-Y., Adhikari, A., Tye, K.M., Frank, L.M. & Deisseroth, K.D. (2012). A prefrontal cortex-brainstem neuronal projection that controls response to behavioral challenge. Nature 492:428-432.

Weissbourd, B., Ren, J., DeLoach, K.E., Guenthner, C.J., Miyamichi, K. & Luo, L. (2014). Presynaptic partners of dorsal raphe serotonergic and GABAergic neurons. Neuron 83:645-662.

Weissmann-Nanopoulos, D., Mach, E., Magre, J., Demassey, Y. & Pujol, J. F. (1985). Evidence for the localization of 5HT1A binding sites on 5-HT containing neurons in the raphe dorsalis and raphe centralis nuclei of the rat brain. Neurochem Int 7:1061-1072.

Womelsdorf, T., Valiente, T.A., Sahin, N.T., Miller, K.J. & Tiesinga, P. (2014). Dynamic circuit motifs underlying rhythmic gain control, gating and integration. Nat Neurosci 17:1031-1039.

Yang, Y., Cui, Y., Sang, K., Dong, Y., Ni, Z., Ma, S. & Hu, H. (2018). Ketamine blocks bursting in the lateral habenula to rapidly relieve depression. Nature 554:317-322.

Zhang, Y.-P. & Oertner, T.G. (2007). Optical induction of synaptic plasticity using a light-sensitive channel. Nat Methods 4:139-141.

Zhong, W., Li, Y., Feng, Q., Luo, M. (2017). Learning and stress shape the reward response patterns of 5-HT neurons. J Neurosci 37:8863-8875.

Zhou, L., Liu, M.-Z., Deng, J., Mu, D. & Sun, Y.-G. (2017). Organization of functional long-range circuits controlling the activity of serotonergic neurons in the dorsal raphe nucleus. Cell Rep 18:3018-3032.

Methods

Viral Constructs and Retrograde Tracer

Construct	Source	Titre (IU/µl)
AAV9.CAG.hChR2(H134R)-mCherry.WPRE.SV40	*(Penn Vector Core, AV-9-20938M)*	*~10^12*
AAV9.Ef1a.DIO.ChETA(E123T/H134R)-eYFP.WPRE.hGH	*(Penn Vector Core, AV-9-26968P)*	*~10^12*
rAAV2-retro-hSyn1-cre	*(Janelia Farm Research Campus)*	*~10^13*
AAV2/9.emCBA.eGFP	*Canadian Neuorphotonics Platform, University of Laval*	*~10^13*

Animal use
SERTcre: B6.Cg-Tg(Slc6a4- cre)ET33Gsat/Mmcd
R26R-TdT: Rosa26R-TdTomato fluorescent protein (TdT) reporter mice

All experiments and procedures were performed in accordance with approved procedures and guidelines set forth by the University of Ottawa Animal Care and Veterinary Services. For this study, SERTcre mice were crossed with the R26R line to generate a SERTcre-TdT mouse line. Mice were kept on a 12:12 hour light/dark cycle, with access to food and water ad libitum unless otherwise noted. A mix of male and female SERTcre-TdT mice (1-3 months for slice physiology experiments, 2-6 months for behavior experiments) were used.

For the behavior portion of the study, mice with a C57BL/6 background were utilized, either originating as mice with a wild-type genotype originating from the SERT-CRE-tdTomato line, or as mice purchased from Charles River Labs. Mice were kept on a 12:12 hour reverse light/dark cycle and were water restricted to 85-90% of their initial weight during behavioral testing.

Slice physiology

Stereotaxic Injections
All experiments and procedures were performed in accordance with approved procedures and guidelines set forth by the University of Ottawa Animal Care and Veterinary Services. For stereotaxic injections, mice were injected with 0.05 mg/kg buprenorphine and anesthetized by inhalation of isoflurane. Injections were performed using a 10 µl Hamilton syringe with a 33 gauge needle and 0.4 - 0.5 µl was injected per coordinate. The virus was injected at a rate of 0.1 – 0.2 ul per minute. Stereotaxic co-ordinates are as follows: LHb (from Bregma skull landmark, in mm: AP -1.7, ML +/- 0.4, DV -3.0) and DRN (from Lambda skull landmark, in mm, 20 degree angle: AP +0.5, ML +1.0, DV -3.0). For retrograde tracing, 0.4 µl of rAAV-retro-TdTomato was injected. For ChR2 (H134R) expression, 0.4 µl of AAV9.CAG.hChR2(H134R)-mCherry.WPRE.SV40 (titre ~10^{12} GC/mL) was injected bilaterally and animals were left to recover for 3 to 4 weeks prior to ex-vivo electrophysiological recordings. In anterograde tracing, AAV-GFP was injected in the LHb and animals were perfused 2-3 weeks post-injections. For experiments requiring sparsely labeled cells in the DRN with ChETA-YFP, we further diluted virus in a 20 % mannitol/saline solution at a ratio of 2:1 (mannitol solution: virus solution). In these experiments, the virus solution was AAV9.Ef1a.DIO.ChETA(E123T/H134R)-

eYFP.WPRE.hGH. The mixed mannitol and virus solution was then injected in the DRN at the coordinates above.

Slice preparation

LHb and DRN containing brainstem slices were prepared from 8 to 10 week old mice (3 to 4 weeks post-stereotaxic injections). For electrical stimulation experiments, brainstem slices were instead prepared from P21-P30 mice. Acute slices were prepared similarly to previously described methods (Geddes et al., 2016). In brief, mice were anesthetized by isoflurane inhalation (Baxter Corporation, Canada) and sacrificed by decapitation. The brain was removed and brain slices were sectioned while immersed in ice-cold choline chloride-based cutting solution of the following composition (in mM): 119 choline-Cl, 2.5 KCl, 1 CaCl2, 4.3 MgSO4-7H2O, 1 NaH2PO4, 1.3 sodium L-ascorbate, 26.2 NaHCO3, and 11 glucose, and equilibrated with 95% O2, 5% CO2. Slices were recovered in a chamber containing standard Ringer's solution of the following composition (in mM): 119 NaCl, 2.5 CaCl2, 1.3 MgSO4-7H2O, 1 NaH2PO4, 26.2 NaHCO3, and 11 glucose, at a temperature of 37°C, continuously bubbled with a mixture of 95% O2, 5% CO2. Slices were left to recover for 1 hour in a recovery chamber and equilibrate to a temperature of approximately 21°C until recordings were performed.

Whole-Cell Electrophysiology

DRN neurons were visualized using an upright microscope: (1) Examiner D1 equipped with Dodt-contrast or differential-interference contrast (DIC) (Zeiss, Oberkochen, Germany; 40x/ 0.75NA objective) or, (2) BX51W1 equipped with DIC optics (Olympus, Center Valley, PA; 40x/ 0.80NA objective). 5-HT neurons were visually identified by TdTomato signal driven by the SERT promoter under EPI-fluorescence illumination (xCite Series 120pc). Whole-cell recordings were carried out using an Axon Multiclamp 700B amplifier, sampled at 10 kHz, digitized with an Axon Digidata 1440A (or 1550) digitizer and filtered at 2 kHz. Whole-cell recordings were performed using borosilicate glass patch electrodes (3-6 MΩ; World Precision Instruments, Florida) pulled on a Narishige PC-10 pipette puller (Narishige, Japan). All experiments were performed at room temperature (except electrical stimulation experiments, conducted at a measured 30-32°C through the use of an in-line bath heater and stage heater.) Slices received constant bath application of Ringer containing (in mM): 119 NaCl, 2.5 KCl, 1.3 MgSO4, 2.5 CaCl2, 1.0 NaH2PO4, 11 glucose, 26.2 NaHCO3, and 0.1 L-Tryptophan saturated with 95% O2 and 5% CO2 (pH = 7.3; 295-310 mOsm/L). Excitatory post-synaptic currents (EPSCs) were recorded using an intracellular solution of either of the following compositions: (1) 115 mM cesium methane-sulfonate, 5 mM tetraethylammonium-Cl, 10 mM sodium phosphocreatine, 20 mM HEPES, 2.8 mM NaCl, 5 mM QX-314, 0.4 mM EGTA, 3 mM ATP(Mg2+), and 0.5 mM GTP, pH 7.25 (adjusted with CsOH; osmolarity, 280–290 mOsmol/L). (2) For 5HT1AR current recordings, an internal solution of the following composition was used: 115 mM potassium gluconate, 20 mM KCl, 10 mM sodium phosphocreatine, 10 mM HEPES, 4 mM ATP(Mg2+), and 0.5 mM GTP, pH 7.25 (adjusted with KOH; osmolarity, 280–290 mOsmol/L). For all voltage clamp recordings, access resistance was continuously monitored using a 125 ms, 2 mV hyperpolarizing pulse, at least 245 ms prior to stimulation. Recordings were discarded when the access resistance changed by >30%. Liquid junction potential was not compensated for.

LED Photostimulation

LED photostimulation was delivered using a PlexBright LED module and controller (465 nm; Plexon, Texas). Light was delivered through a 200 μm patch fiber cable with a bare fiber tip with ~ 1 cm of glass exposed. For EPSC/EPSP stimulation, unless otherwise stated, optically evoked-PSCs were stimulated at a frequency of 0.1 or 0.067 Hz with light pulses of 1-3 ms in length and an irradiance of 792 mW/mm2. In driving 5-HT1A-mediated currents, optical stimulation was accomplished using 10 ms pulses at 20 Hz for 400 ms at an irradiance of 792 mW/mm^2.

Immunohistochemistry

Mice were perfused using a minimally invasive method developed by Kenneth D. Eichenbaum and colleague in 2005. Briefly, mice were put under general anaesthesia with 1.5% isoflurane. The animal was then placed on its back for injection (1 mL PFA4% in 0.1 M PBS). The injection was done with a 1 mL syringes equipped with a 26G needle over a 30 seconds course. The correct position of the needle was confirmed by the appearance of blood in the needle hub. Brains were then put in 10 mL of PFA4% overnight and then transferred in a 15 mL tube with 10 mL of PBS (0.1 M PBS, 0.1% Sodium azide). The fixed brains were then cut in 50 um thick slices with a vibrotome (Vibrotome,1500 sectioning system).

Free-floating sections were blocked in 1% BSA + 0.03% Triton X-100 (TX-100) for 45-60 min, and incubated in primary antibody in blocking solution at 4 °C. On the following morning, slices were washed three times, for 5 min each time, with 0.1% Tx-100 before incubation in the secondary antibody goat anti-rabbit–conjugated Alexa-647 (Life technologies, A21245) for 2 h at room temperature. Slices were washed with 0.1% Tx-100 three times, for 5 min each time, before mounting onto slides with Fluoromount-G (Southern Biothech, 0100-01). The primary antibody used for this paper were Tryptophan hydroxylase 2 (1:1,000; Millipore, ABN60), NeuN (1:1000; EnCor Biotechnology, RPCA-Fox3-AP) and Nissl (1:1000; NeuroTrace® 435/455 Blue Fluorescent Nissl Stain, Life technologies, N21479).

Fluorescent tracer injections in DRN

To examine the local connectivity and network structure in DRN, we performed visually guided injections of fluorescent tracer in DRN in acute slices (described fully in Trinh et al., 2015). Briefly, in these experiments, SERT-CRE-tdTomato animals (P30-P40) were sacrificed and acute slices prepared as described above (*slice preparation*). At 5x-10x magnification with a Zeiss upright microscope with an epifluorescent lamp, Alexa Fluor 488 dextran (suspended at 10 mg/mL in 0.1M phosphate-buffered saline (PBS) pH 7.2) was injected in DRN by iontophoresis (five to ten 400 ms pulses of ~ –100 V via a 7 mOhm electrode). After a fluorescent sphere of <50 µm diameter was observed, injection was stopped. Slices were incubated overnight in oxygenated ACSF to allow anterograde and retrograde transport, fixed in 4% paraformaldehyde and rendered transparent using the SeeDB procedure (see Trinh et al., 2015 for details). Slices were imaged with a Zeiss confocal microscope (LSM800 AxioObserver Z1 microscope; Zen software).

Electrical stimulation of 5-HT afferents

Electrical stimuli were delivered through a bipolar concentric stimulating electrode located >100 um from the soma of the recorded neuron. Stimuli were 0.1 ms in duration, and consisted of frequencies provided in the text. For all electrical stimulation experiments, we bath-applied a cocktail of synaptic blockers to isolate the 5-HT1AR response (10 µM NBQX, 100 µM picrotoxin, 200 nM CGP 55845). Additionally, for these experiments, a K+MeSO4 internal solution with 10 uM BAPTA was utilized to prevent the after-hyperpolarization of action potentials from interfering with the recorded 5-HT1AR responses. All 5-HT electrical stimulation experiments were performed at near-physiological temperature (30-32 °C).

Data Analysis

All electrophysiological recordings were analyzed offline using Clampfit 10.4 (Molecular Devices), Origin 8.5 software (OriginLab) and the Numpy and Scipy computational packages within Python. All data are presented as means +/- SEM. n refers to the number of cells recorded. Unless otherwise stated, statistical significances were derived using a standard Student's two-sided t-test ($p < 0.05$). P values of less than 0.05 were considered statistically significant and are indicated with an asterisk(*). Unless otherwise stated, all measurements were taken from distinct neurons.

Drugs and Chemicals
Picrotoxin, 2,3-Dioxo-6-nitro-1,2,3,4-tetrahydrobenzo[f]quinoxaline-7-sulfonamide di-sodium salt (NBQX), DL-2-Amino-5-phosphonopentanoic acid (D,L-APV), picrotoxin, CGP 55845 and WAY 100-635 were purchased from Abcam (Cambridge, MA). Tetrodotoxin (TTX) was purchased from Tocris Bioscience (Ellisville, MO). 4-Aminopuridine (4-AP) was purchased from Sigma Aldrich (St. Louis, MO).

Modeling of synaptic dynamics and network simulations

GIRK conductance
The GIRK conductance kinetics were modelled as a sum of exponentials:

$$g_{GIRK}(t \mid a, \tau_{decay}, \tau_{rise}) = a(e^{-t/\tau_{decay}} - e^{-t/\tau_{rise}}) \quad (1)$$

where $\tau_{decay} > \tau_{rise}$ and $t > 0$.

The parameters $a, \tau_{decay}, \tau_{rise}$ were fit to single-pulse electrical stimulation data (n=6 neurons) using a least-squares approach as follows: We first fit a monoexponential decay function $f(t \mid \tau_{decay}) = e^{-t/\tau_{decay}}$ to the normalized post-peak decay phase of $g^{exp}_{GIRK}(t)$. This yielded a constrained estimate of the GIRK decay, $\hat{\tau}_{decay}$. Next, fixing τ_{decay} , we found the values of $\hat{a}, \hat{\tau}_{rise}$ that minimized the mean-squared error over the whole observation period.

Each estimate was averaged across the population (n=6 neurons):

$$\hat{a} = 0.725\ nS$$
$$\hat{\tau}_{decay} = 308.04\ ms$$
$$\hat{\tau}_{rise} = 85.97\ ms$$

These spike triggered changes in conductances were simulated numerically using their equivalent in linear differential equations.

Quantifying 5-HT release dynamics through optogenetic stimulation
In some experiments, we optogenetically stimulated CHETA-expressing 5-HT neurons in slice, while recording 5-HT1AR outward currents from identified 5-HT neurons. By photostimulating at 20Hz and varying the optical pulse number, we could infer basic properties of release dynamics at these serotonin-serotonin synapses.

We assume that the current generated by a single pulse is a random variable following a binomial distribution $B(n, p)$, which reflects the activity of n independent serotonin-serotonin synapses with release probability p. For a train of successive pulses, we assume p and n are fixed, and that each pulse is independent. Then $Q(n_{pulse} = a)$, the distribution of currents given by a pulses, is distributed as a sum of a binomial distributions:

$$Q(n_{pulse} = a) \sim B(a \cdot n, p)$$

Accordingly, the variance of Q as the pulse number a varies is as follows (Sigworth, 1980):

$$\mathrm{var}[Q(n_{pulse} = a)] = (p(1-p)n)a + \mathrm{noise} \quad (2)$$

Since the variance of the current does not change as a function of pulse number (Fig. S6), we can conclude that the release probability is close to $p = 1$. This probably reflects the artefactual increase in release probability obtained when optogenetically activating synaptic terminals (Zhang & Oertner, 2007), necessitating other approaches to determine release probability under naturalistic conditions (see the section below).

Quantifying 5-HT release dynamics through electrical stimulation

We additionally performed experiments where 5-HT afferents were electrically stimulated in acute slice preparations while recording from identified 5-HT neurons. Electrical stimulation intensities were low (in the perithreshold response range), and stimulation frequency was 1Hz. To quantify successes and failures, we computed the total event charge triggered by each stimuli (by integrating current over time), which formed an *event* distribution containing both putative successes and failures. We constructed a surrogate *noise* distribution by performing an identical analysis on a nonstimulated portion of the same recording for each neuron (*ie* integrating equivalent durations of membrane noise where no stimuli were presented). Next, for each neuron we transformed the *event* and *noise* charge distributions into z-scored distributions (where the z-score was always computed from that neuron's *noise* distribution). Finally, we pooled z-scored distributions across neurons. This allows us to directly compare electrically evoked responses; for example, responses with a z-score > 3 likely represent successes, while responses with a z-score near 0 probably represent release failures. For electrical stimulation at higher frequencies (1-20Hz), we constructed surrogate noise distributions and event distributions in a manner identical to that described above.

For paired-pulse and pulse-chase stimuli, we quantified responses by first computing total charge elicited over the duration of each of the stimuli (integrating current over time). We next computed the total charge elicited by a single electrical stimulation delivered in isolation, and used this to calculate an expected value for purely linear summation of two pulses (*ie* by multiplying the single stimulation-induced charge by 2). Finally, for each neuron, we normalized the stimulus-evoked charges in the paired-pulse or pulse-chase condition by the expected value for linear summation of two individual pulses.

Short-term plasticity

Short-term plasticity dynamics were modeled using a linear-nonlinear approach called the spike-response plasticity (SRP; Rossbroich et al., 2021). It utilizes a possibly complex efficacy kernel to capture spike-triggered changes in short-term plasticity. Namely, each presynaptic spike is convolved with the following efficacy kernel:

$$\mathbf{k}_{\mu}(t) = a_s e^{-t/\tau_s} + a_l(e^{-t/\tau_l^+} - e^{-t/\tau_l^-}) \quad (3)$$

This kernel consists of multiple timescales of responses. The short component is controlled by τ_s and a_s, and dictates the rapid short-term facilitation dynamics. The long component is controlled by τ_l^+ and a_l, and dictates the more prolonged short-term depression dynamics. τ_l^- is a shaping term that reduces the effect of short-term depression in the early post-spike phases where short-term facilitation dominates. Since the kernel consists of a sum of exponential functions, it can be conveniently written as a dynamical system. Let k reflects the

current efficacy state of the synapse ($k = \mathbf{k}_\mu * S$) and is transformed through a nonlinear operation into a spike efficacy, μ. In turn, μ dictates the magnitude of the postsynaptic response given a presynaptic spike, and is implemented as a nonlinear readout of k:

$$f(x) = \frac{1}{1+e^{-x}}$$
$$\mu = \frac{1}{f(b)} f(k+b) \tag{4}$$

Here, $f(x)$ is the nonlinear function and b is a baseline term that controls whether the STP dynamics evolve sublinearly or supralinearly.

Fitting short-term plasticity dynamics to experimental data

We start with a set of paired-pulse electrical stimulation experiments where the time interval ranges from 50ms to 1sec. For our experimental dataset, we had computed, for each time interval t_i, a ratio of the total charge transfer for both pulses q_1 and q_2 to the charge transfer for a single pulse delivered separately:

$$R(t_i) = \frac{q_1 + q_2}{q_1} = \frac{\mu_1 + \mu_2(t_i)}{\mu_1} \tag{5}$$

Where μ_1 and μ_2 relative postsynaptic response amplitudes for the first and second pulse given by the SRP model. We wish to find optimal parameters for the efficacy kernel, $\mathbf{k}_\mu(t \mid a_s, a_l, \tau_s, \tau_l^+, \tau_l^-)$, such that we arrive at a local minimum in a cost function comparing the experimental and theoretical charges for various delays τ_i of the paired-pulse stimulation.

We start by deriving an analytical expression for (5) in terms of the underlying efficacy kernel. The first spike's efficacy is taken by evaluating the efficacy kernel at time 0:

$$\mu_1 = \frac{1}{f(b)} f(\mathbf{k}_\mu(t=0) + b)$$
$$\mu_1 = \frac{1}{f(b)} f(a_s + b) \tag{6}$$

The second spike's efficacy is taken by evaluating the sum of an efficacy kernel at time t_i (efficacy from first spike at the time of spike two) and an efficacy kernel at time 0 (second spike's efficacy).

$$\mu_2 = \frac{1}{f(b)} f(\mathbf{k}_\mu(t=0) + \mathbf{k}_\mu(t=t_i) + b)$$
$$\mu_2 = \frac{1}{f(b)} f(a_s(1 + e^{-t_i/\tau_s}) + a_l(e^{-t_i/\tau_l^+} - e^{-t_i/\tau_l^-}) + b) \tag{7}$$

Substituting (6) and (7) into (5):

$$R(t_i) = \frac{\frac{1}{f(b)} f(a_s + b) + \frac{1}{f(b)} f(a_s(1 + e^{-t_i/\tau_s}) + a_l(e^{-t_i/\tau_l^+} - e^{-t_i/\tau_l^-}) + b)}{\frac{1}{f(b)} f(a_s + b)}$$

$$R(t_i) = \frac{f(a_s + b) + f(a_s(1 + e^{-t_i/\tau_s}) + a_l(e^{-t_i/\tau_l^+} - e^{-t_i/\tau_l^-}) + b)}{f(a_s + b)} \quad (8)$$

Equation (8) and the corresponding experimental results (5) are used to perform least-squares optimization on the parameters $a_s, a_l, \tau_s, \tau_l^+, \tau_l^-, b$. This yields the following parameter estimates:

$$a_s = 1.11$$
$$a_l = -1.80$$
$$\tau_s = 0.128 \text{ s}$$
$$\tau_l^+ = 1.27 \text{ s}$$
$$\tau_l^- = 0.698 \text{ s}$$
$$b = -6.22$$

A general expression for spike efficacy given past spiking history

One can also write a solution to the generalized case of calculating the efficacy, μ_n, of a certain presynaptic spike n occurring at time t_n, given a past history of spikes with times $t_1, t_2, t_3, \ldots t_{n-1}$:

$$\mu_n = \frac{1}{f(b)} f(\sum_{s=1}^{n} \mathbf{k}_\mu(t = t_n - t_s)) \quad (9)$$

This equation is used to calculate the model's predictions for the matched pulse-chase experimental data.

Computational model of DRN network with recurrent GIRK-coupled 5-HT1AR connectivity, receiving LHb input.

To construct a simplified model of the DRN network, we took a modular approach where each individual component was fitted to experimental data where possible.

Individual 5-HT neurons were fit with a simplified leaky-integrate-and-fire model. The fitting was performed experimentally according to previously described methods (Pozzorini et al., 2015). Briefly, identified serotonin neurons from SERT-CRE-tdTomato mice were recorded in whole-cell current-clamp configuration, and a noisy input stimulus was presented through multiple test and training repetitions. These repetitions were used to train a generalized integrate-and-fire model to each individual serotonin neuron by maximizing the likelihood of the model (for full details, see Harkin et al., 2021).

In this work we focused on basic extracted parameters from this model: $g_{leak}, E_{leak}, C_m, t_{refractory}, V_{thresh}$. While Harkin et al., (2021) utilized a current-based generalized-integrate-and-fire model to represent serotonin neuron firing, here we consider a simplified, conductance-based, leaky-integrate-and-fire model of individual serotonin neurons:

$$\frac{dV}{dt} = \frac{-g_{leak}(V - E_{leak}) - g_{LHb}(V - E_{AMPA}) - g_{pois}(V - E_{AMPA}) - g_{GIRK}(V - E_K) - g_{AHP}^{tot}(v - E_K) - I_{const}}{C_m}$$

(10)

With the fitted parameters:

$$g_{leak} = 1.4 \text{ nS}$$
$$C_m = 0.0876 \text{ nF}$$
$$t_{refractory} = 6.5 \text{ ms}$$
$$V_{thresh} = -52.33 \text{ mV}$$

And the chosen ionic reversal potentials, which, for the purposes of this LIF model, are considered as fixed meta-parameters:

$$E_{leak} = -68.07 \text{ mV}$$
$$E_K = -90 \text{ mV}$$
$$E_{excit} = 0 \text{ mV}$$

Conductances for $g_{LHb}, g_{pois}, g_{GIRK}, g_{AHP}$ were considered with the following dynamics, where s is a synapse state variable which instantaneously increments by 1 whenever a presynaptic neuron fires, and exponentially decays to 0 with a characteristic time-constant:

$$g_x = s_x \cdot g_x^{unitary}$$
$$\frac{ds}{dt} = \frac{-s_x}{\tau_x} \qquad (11)$$

where x represents conductances of either *LHb*, *pois*, *GIRK* or *AHP*.

The AHP conductance is expressed as a sum of three unitary conductances with distinct timescales.

$$g_{AHP}^{tot} = s_{AHP}^{slow} g_{AHP}^{slow} + s_{AHP}^{med} g_{AHP}^{med} + s_{AHP}^{fast} g_{AHP}^{fast} \qquad (12).$$

The following values were chosen for individual parameters of the model. Note that excitatory decays were chosen to reflect a mixture of both AMPA and NMDA currents. Note that these reflect unitary conductance values, and neurons receive multiple LHb (g_{LHb}) and recurrent GIRK (g_{GIRK}) inputs, as well as a constant background rate of Poisson inputs (g_{pois}).

$$g_{LHb} \sim N(\mu = 1.5,\ \sigma = 0.2) \text{ nS}$$
$$g_{pois} \sim N(\mu = 0.5,\ \sigma = 0.1) \text{ nS}$$
$$g_{GIRK} = 0.01 \text{ nS}$$
$$I_{const} \sim N(\mu = 10,\ \sigma = 5) \text{ pA}$$
$$\lambda_{pois} = 25 \text{ Hz}$$
$$\tau_{A+N} = 20 \text{ ms}$$
$$\tau_{GIRK} = 50 \text{ ms}$$

For the AHP dynamics, the following values were extracted from fits on identified 5-HT neurons using a previously described protocol (see Pozzorini et al., 2015; Harkin et al. 2021):

$$\tau_{AHP}^{fast} = 3 \text{ ms}$$
$$\tau_{AHP}^{med} = 30 \text{ ms}$$
$$\tau_{AHP}^{slow} = 300 \text{ ms}$$
$$g_{AHP}^{fast} = \frac{0.0281 \text{ nA}}{V_{thresh} - E_k}$$
$$g_{AHP}^{med} = \frac{0.0333 \text{ nA}}{V_{thresh} - E_k}$$
$$g_{AHP}^{slow} = \frac{0.0210 \text{ nA}}{V_{thresh} - E_k}$$

Note that since the generalized integrate-and-fire model in Pozzorini et al. (2015) extracts a spike-triggered current for the AHP, we convert this to a conductance by dividing by the driving force at spike threshold.

The DRN network model consisted of 5000 5-HT neurons with the LIF dynamics described above. 5-HT neurons were recurrently connected in an unstructured manner with 0.5% random connection probability and 0.1 nS unitary GIRK synaptic conductance ($\sum 2.5$ nS net GIRK inhibition received by each neuron before facilitation/depression dynamics are considered). Short-term plasticity between 5-HT neuron connections was modelled using the linear-nonlinear description fit to data, described in the preceding section. 25% of DRN 5-HT neurons receive long-range input from a cluster of 500 LHb neurons emitting Poisson spiketrains at rates specified in the text, where each LHb neuron and 5-HT neuron is randomly connected with 1% probability (*ie* each 5-HT neuron receives an average of 5 LHb synapses) with synapse strength specified above. This yields a mean LHb conductance of $\sum 7.5$ nS for each 5-HT neuron.

<u>Computational model of DRN network with recurrent GIRK-coupled 5-HT1AR connectivity, receiving LHb and Area X input.</u>

In some simulations (Fig. 6), we considered a DRN network where 25% of neurons received LHb input, and 25% of neurons received input from a generic area termed Area X. In

these simulations, the basic neural architecture and dynamics were identical to that described above, except that 25% of 5-HT neurons now received input from Area X (non-overlapping with the 25% of neurons already receiving LHb input). Area X consisted of 500 neurons emitting Poisson spikes at rates specified in the text, where each X neuron and 5-HT neuron is randomly connected with 1% probability (*ie* each 5-HT neuron receives an average of 5 X synapses). This yields a mean X conductance of $\sum 7.5$ nS for each 5-HT neuron. Synapse strength is identical to that of LHb-5-HT synapses, as are decay kinetics:

$$g_X \sim N(\mu = 1.5,\ \sigma = 0.2) \text{ nS}$$
$$\tau_{A+N} = 20 \text{ ms}$$

Auditory classical conditioning task

Surgery

All experiments and procedures were performed in accordance with approved procedures and guidelines set forth by the University of Ottawa Animal Care and Veterinary Services. For stereotaxic injections, mice were injected with 0.05 mg/kg buprenorphine 1 hour prior to surgery and anesthetized by inhalation of isoflurane (4% for induction and 1.5-2% for maintenance). The head was shaved, ointment was applied to each eye, and an incision was made above the skull. A dental drill was used to perform skull craniotomies at locations above the coordinates for LHb and DRN described below.

For stereotaxic injections in LHb, we utilized the virus AAV9.CAG.hChR2(H134R)-mCherry.WPRE.SV40 at a concentration of ~10^{-12} GC/mL. Injections were performed using a 10 µl Hamilton Neuros syringe with point style 4 (12° beveled needle point). 0.4 - 0.5 µl was injected per coordinate at a rate of 0.1 – 0.2 µl per minute. Stereotaxic coordinates for injection are as follows for LHb, from Bregma skull landmark, in mm: AP +1.7, ML +/- 0.4, DV -3.1 to -3.3. Following stereotaxic injections, we affixed a custom stainless steel or 3D-printed Acrylonitrile butadiene styrene (ABS) headbar to the anterior surface of the skull with C&B Metabond Quick Adhesive Cement (Parkell).

For optic fiber implantation in DRN, each animal received a fiber (Doric Mono Fibre-Optic Cannula, 4mm length, part number: MFC_100/125-0.37_4mm_ZF1.25_C45) which was implanted at the following coordinates, from Bregma skull landmark in mm: AP-4.6, ML 0, DV -2.9. In some animals, we used an angled injection to avoid the superior saggital sinus (20° angle, from Bregma skull landmark in mm: AP-4.6, ML +1, DV -3.25). Optic fibers were slowly lowered to the desired dorsoventral location, and affixed with C&B Metabond Quick Adhesive Cement (Parkell) followed by Jet Denture repair cement (Lang) to provide structural stability to the implant.

After surgery, animals received topical bupivicaine (2%) and intraperitoneal (IP) carprofen (20 mg/kg). Post-operative care consisted of a further bupivicaine treatment at 4-6h post-surgery, and IP carprofen injection 4-6h post-surgery and for the next two days. Animals were allowed to recover from surgery for one week before water restriction was started. All animals were housed separately.

Behavior and water restriction

Animals were placed on water restriction for 7 days prior to the start of the task. During this time, they were habituated to the experimenters and the apparatus through handling and brief periods of head fixation while daily water (0.8 - 1 mL) was provided. After habituation, for 2-3 days each mouse was head-fixed for short bouts and 5-10 uL apple juice was delivered to a

lickport every 1 to 8 s without preceding auditory tones. Following this, mice underwent 1-2 weeks of training on the primary auditory classical conditioning task, described below.

The auditory classical conditioning task consisted of 120 randomly interleaved trials presented to each mouse per day, giving a total reward value of ~0.6 - 0.8 mL per mouse per day. Inter-trial intervals were drawn from an exponential distribution with $\lambda = 5$ s, where 2 s $<$ ITI < 14 s to prevent excessively long or short ITIs. Exponentially distributed ITIs give the convenient property that trials follow a Poisson distribution in time, and therefore are memoryless (the mice cannot predict trial onset times). To prevent the mice from licking continuously during the baseline periods, new trial starts were contingent on baseline mouse licking of <10% (fractional time). Three trial types were randomly interleaved: a *large-reward trial*, consisting of a 3 kHz tone and a 10uL apple juice reward, a *small-reward trial*, consisting of a 6 kHz tone and 5 uL apple juice reward, and a *no-reward trial*, consisting of a 12 kHz tone and 0 uL apple juice reward. For each trial, the tone lasted 1 s, the trace period between tone and reward delivery was drawn from a Gaussian distribution with $\mu = 2$ s, $\sigma = 4$ s (values of $t_{trace} < 0.5$ s were prohibited), and the apple juice reward was concomitantly delivered with a 500 ms white noise tone to aid learning. Following reward delivery, licking was monitored for 4 s before the trial was terminated. This auditory classical conditioning task was presented daily to mice for 1-2 weeks until criterion performance had been achieved for >2 consecutive days. Criterion performance was defined as a mean lickrate of >0.5 Hz during the trace period of large-reward trials. While many mice displayed mean lickrates which were significantly higher than this (Fig. 8C), this was a convenient lower threshold for criterion performance.

After criterion performance was reached, mice experienced the auditory classical conditioning paradigm while we optogenetically activated the habenulo-raphe pathway in some trials. The trial structure consisted of 120 trials of interleaved large-reward, small-reward and no-reward trials as before. Each trial was composed of the same tone and reward associations and durations as described above, except the period between tone and reward was fixed at 2 s. For the first 40 trials, no optogenetic stimulation was delivered (*baseline block*). For the final 80 trials, optogenetic stimulation was delivered on 40 randomly chosen trials (*optogenetic stimulation block*). Optogenetic stimulation was composed of pulses of 10 ms width, at frequencies noted in the text (5Hz or 20Hz), delivered during the period between tone and reward. Optogenetic stimulation was delivered intracranially via an optic fibre implanted in DRN, to which a patch cable was connected before the session.

The behavioral apparatus consisted of a sound-insulated box containing a Raspberry Pi 3B, custom steel head fixation apparatus and equipment for delivering stimuli and acquiring signals. Lick signals were acquired via a custom 3D-printed combined infrared lickometer and stainless steel lickport. Lickport placement was adjusted daily for each mouse to ensure optimal performance and signal acquisition. A solenoid valve (NResearch 2-way NC isolation valve) gated apple juice delivery, and flow rate was calibrated weekly. Speakers connected to the Raspberry Pi (Logitech Z150) delivered auditory stimuli. We visualized animal behavior with an infrared video camera connected to the Raspberry Pi (Raspberry Pi Camera Module 2 NoIR). In vivo optogenetic stimulation was delivered using a PlexBright LED module and controller (either blue light, 465; or yellow light, 590 nm; as noted in the manuscript; Plexon, Texas) and a PlexBright optical patch cable. A custom script (Python 3.8) on the Raspberry Pi registered lickometer data at 200 Hz while controlling trial structure, auditory stimulus delivery, reward delivery and optogenetic stimulation. Data was stored in hdf5 format.

After behavioral testing was completed for individual mice, they were perfused transcardially with 4% paraformaldehyde, and brains were cut in 50-100 um sections. Immunohistochemistry was performed as described above, and the injection sites and optic fiber tracts were verified.

Data analysis

Data was analyzed with custom Python 3.8 scripts, employing the numpy (van der Walt et al., 2011), scipy (Jones et al., 2001), h5py and matplotlib technical computing libraries. Briefly, raw licking data was binarized and converted into lick onset times. For visualizations (Fig. 8E-F), licking signals were calculated by convolving lick onset times with a gaussian kernel ($\sigma = 50$ ms) and averaging across all trials of that type. Optogenetic analyses are described below.

Optogenetically evoked changes in anticipatory (trace) licking were calculated as follows: we considered trials of a given type during the optogenetic stimulation block (last 80 trials), and calculated the mean licking frequency in the period between the tone and reward (anticipatory licking) for each trial. To calculate an optogenetically evoked change in anticipatory licking, the mean anticipatory licking frequency for optogenetically stimulated trials was subtracted from the mean anticipatory licking frequency for non-stimulated interleaved trials during the optogenetic stimulation block. Optogenetically evoked changes in reward licking were calculated in a similar way, but the period considered was the post-reward epoch.

We additionally considered whether optogenetic stimulation modulated behavior beyond the stimulated period (Fig. 8I). For these analyses, we compared nonstimulated trials during the baseline block with nonstimulated interleaved trials during the optogenetic stimulation block. For each trial of a given type, we first computed mean anticipatory licking frequency as described above. Next, to quantify long-term optogenetically evoked changes in anticipatory licking, we subtracted mean anticipatory licking frequency for nonstimulated trials during the optogenetic stimulation block from mean anticipatory licking frequency for trials during the baseline block.

References

Sigworth, F.J. (1980). The variance of sodium current fluctuations at the node of Ranvier. J Physiol 307:97-129.

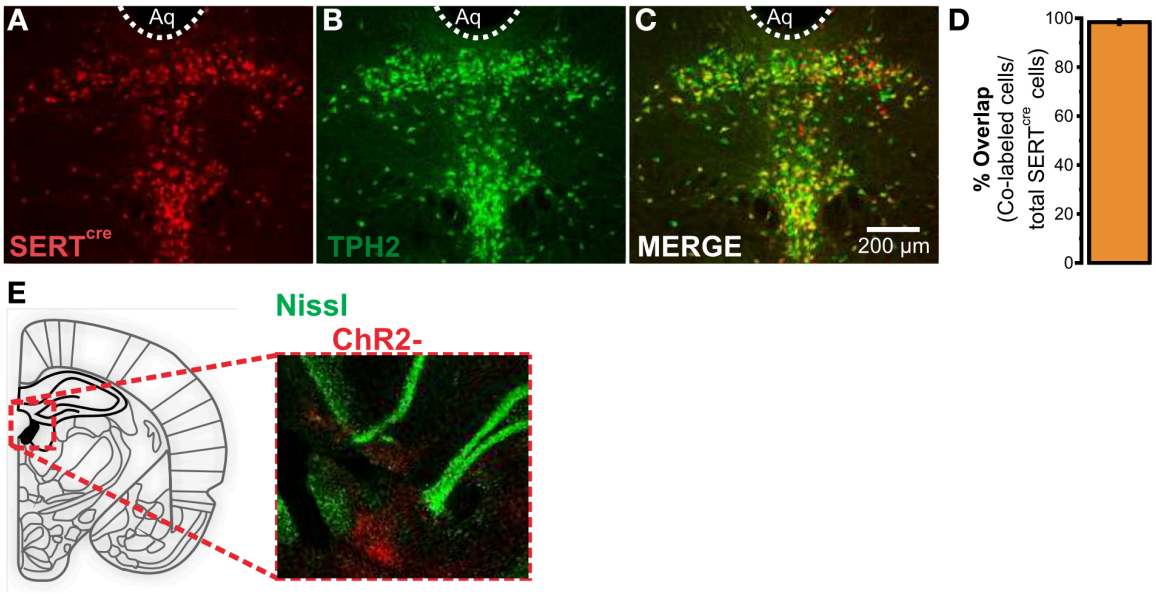

Figure S1: Validation of SERT-CRE-tdTomato mouse line and LHb injection site. Confocal image of SERTcre **(A)** and TPH2-expressing **(B)** 5-HT neurons in the DRN. **(C)** Merge confocal image of SERTcre and TPH2 channels. **(D)** Bar plot of overlap between SERT-cre and TPH2-expressing 5-HT neurons in the DRN (98.38 +/- 0.8; n = 3, mean +- SE). **(E)** Representative image of LHb injection site (AAV-ChR2-mCherry).

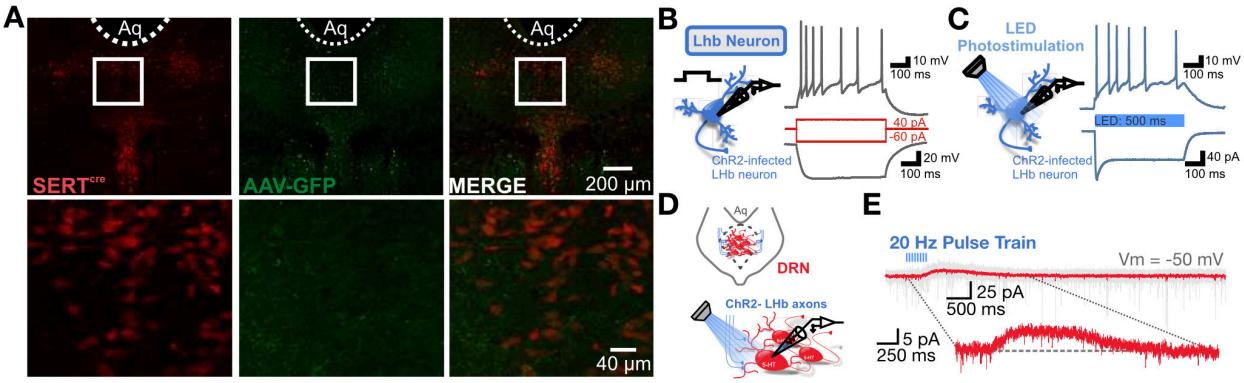

Figure S2: LHb sends axonal projections to the DRN. **(A)** Confocal image of GFP-expressing LHb axons in the DRN with 5-HT neurons identified with SERT-TdT. **(B)** ChR2-infected LHb neuron can be induced to spike with current injection. **(C)** LED photostimulation produces qualitatively similar spiking patterns to those induced by current injection. **(D)** Experimental schematic for long-range optogenetic interrogation. **(E)** Example serotonin neuron which does not receive direct LHb input, but displays a delayed heterosynaptic inhibitory current.

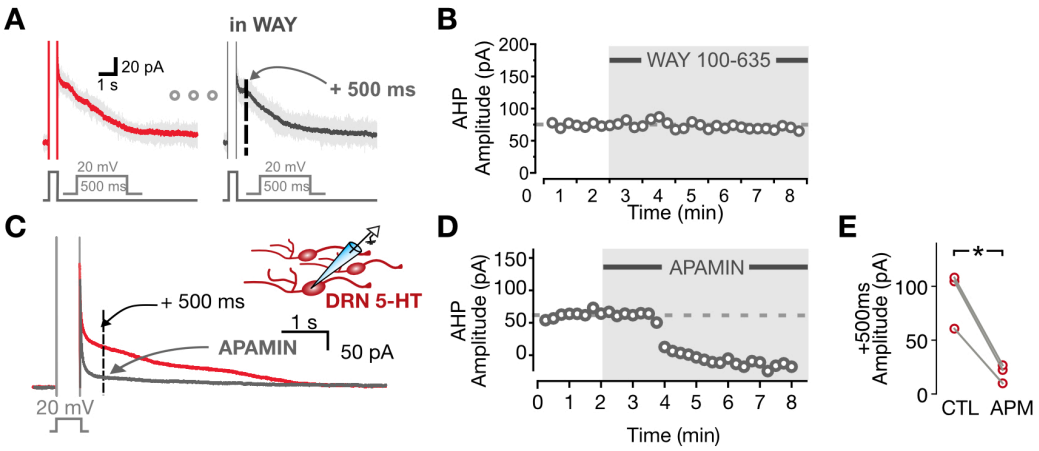

Figure S3: Voltage-clamp experiments provide evidence that the afterhyperpolarization of serotonin neurons is mediated by SK channels, not 5-HT1ARs. **(A)** Representative traces of AHP current (IAHP) driven by a 500 ms depolarization step to 20 mV in voltage clamp. **(B)** Representative scatter plot showing no differences in IAHP amplitude following WAY 100-635 application. **(C)** Representative IAHP traces before and after APAMIN application (300 nM). **(D)** Representative scatter plot showing the IAHP +500 ms amplitudes in response to APAMIN. **(E)** +500 ms IAHP amplitudes before and after APAMIN application (CTL, 91.1 +/- 15.3; APM, 19.6 +/- 5.0; n = 3; p = 0.02, paired two-sided t-test).

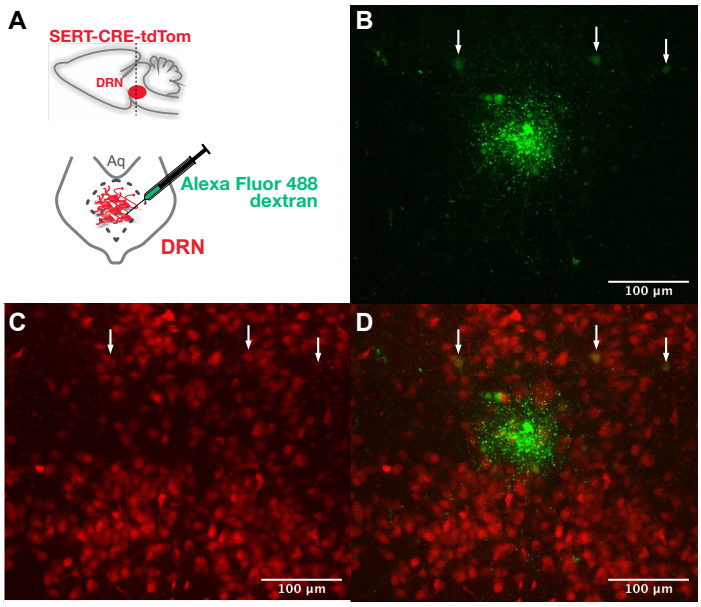

Figure S4: Fluorescent dextran injections in DRN reveal local 5-HT projections. **A)** Experimental schematic illustrating visually guided dextran injections in DRN of acute slices. **B)** Confocal image showing dextran injection site and labeled neurons. **C)** Confocal image showing tdTomato-labeled serotonin neurons. **D)** Overlaid confocal image showing overlap between distant dextran-labeled neurons and tdTomato fluorescence.

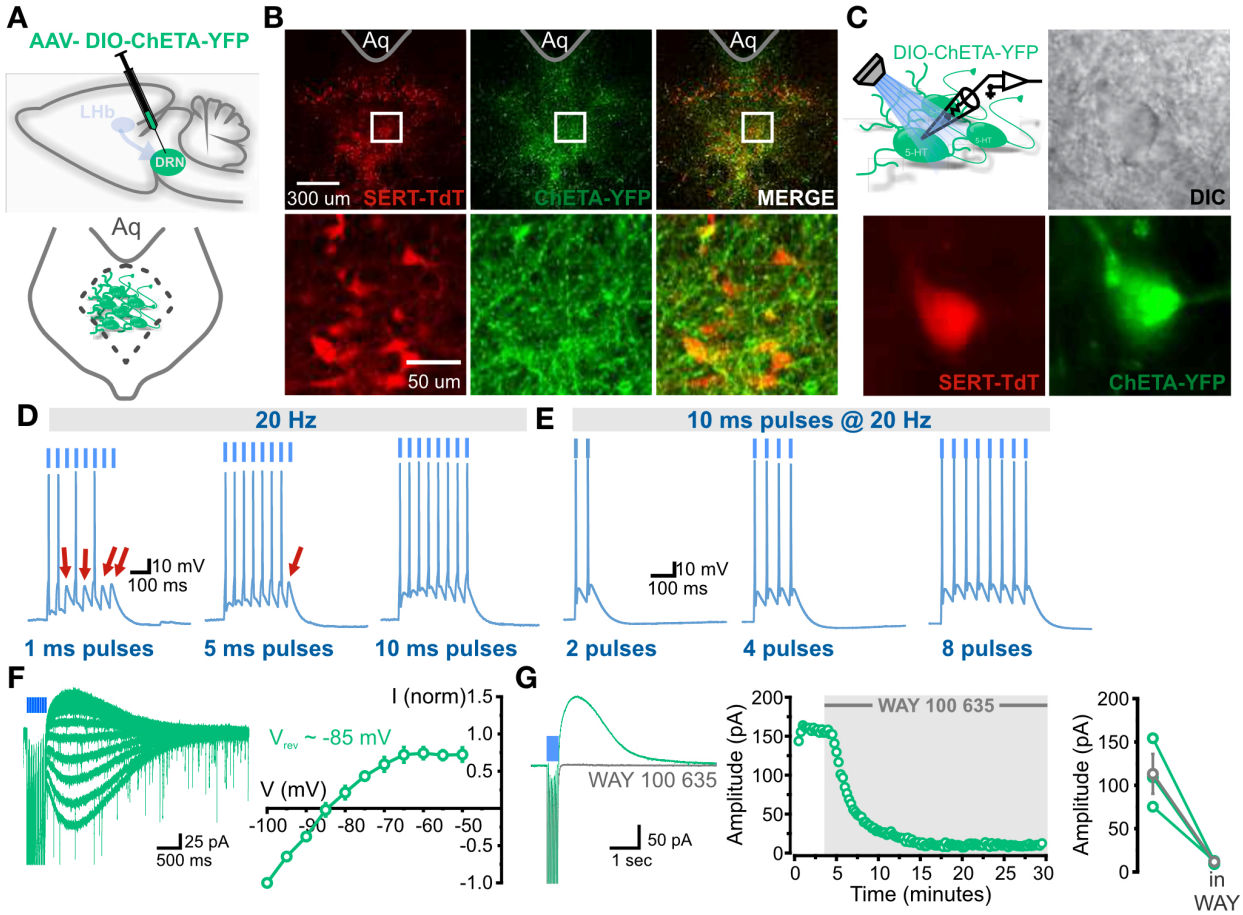

Figure S5: Validation of local CHETA optogenetic strategy in DRN. **(A)** Schematic depicting AAV-DIO-ChETA-YFP injection into the DRN of SERTcre-TdT mice. **(B)** Confocal image of ChETA-YFP expression in tdTomato-positive neurons in the DRN. Above, low magnification (scale, 300 µm) ; below, high magnification (scale, 50 µm). **(C)** Schematic and EPI-flourescent image of whole-cell recordings from ChETA-YFP-expressing SERT-TdT neurons. **(D)** LED stimulation of 5-HT neuron spiking with different pulse durations at frequency of 20 Hz. **(E)** LED stimulation of 5-HT neuron spiking in response to varying number of 10 ms pulses at 20 Hz. **(F)** Representative IV relationship traces and IV relationship (n = 5, mean +- SE). **(G)** Representative traces and scatter plot showing complete blockade of outward current by WAY 100-635. Right, population data is displayed (Pre-WAY, 112.9 +/- 22.9; Post-WAY, 11.5 +/- 1.1; n = 3; p = 0.02, paired two-sided t-test).

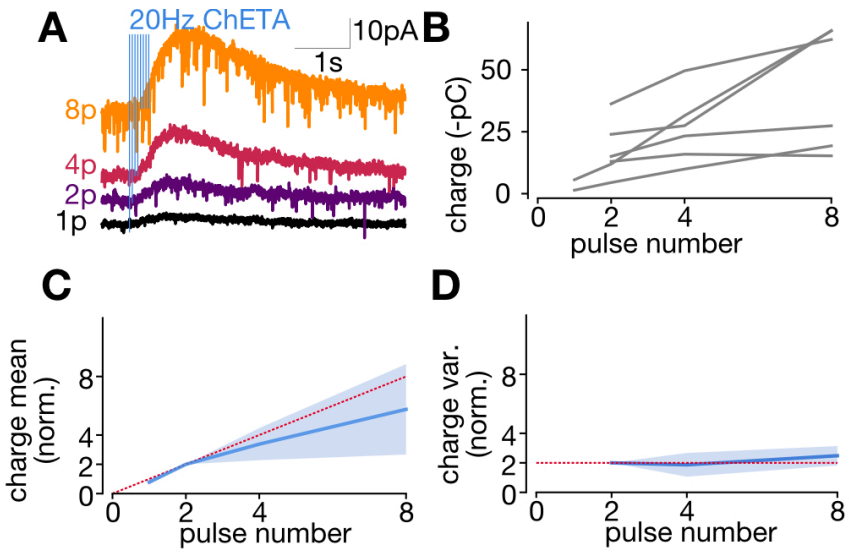

Figure S6: Postsynaptic dynamics of recurrent 5-HT1A connections indicate non-desensitizing receptors. **(A)** Representative averaged traces from a single non-CHETA-expressing 5-HT neuron depicting responses to 20Hz optogenetic stimulation of DRN for various pulse numbers. **(B)** Event charge for each neuron as a function of pulse number at 20Hz (n=6). **(C)** Charge mean as a function of pulse number, normalized to the mean at two pulses (n=6, mean +-SD). Dotted red line represents a linear relationship between pulse number and evoked charge. **(D)** Charge variance as a function of pulse number, normalized to the variance at two pulses (n=3, mean +-SD). Dotted red line represents predicted variance for release probability p=1.

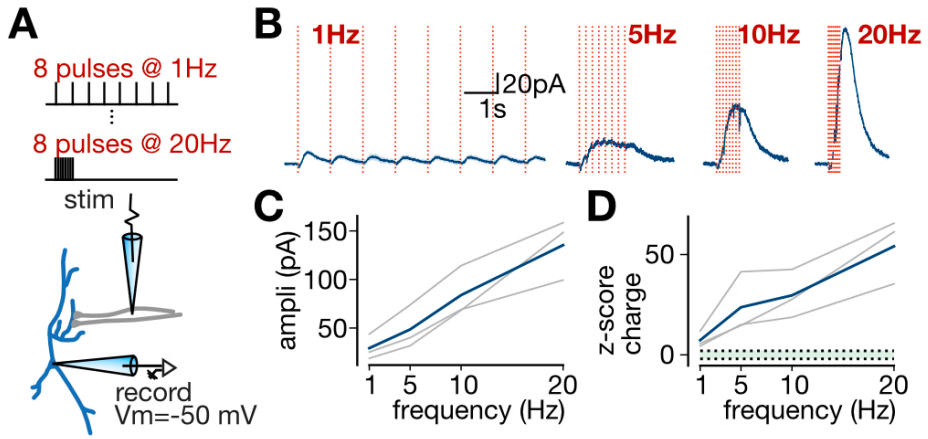

Figure S7. Frequency dependence of 5-HT1A connections at suprathreshold stimulation frequencies. **(A)** Experimental setup depicting electrical stimulation of 5-HT1A synapses while recording from an identified 5-HT neuron in the whole-cell configuration. **(B)** Representative averaged traces from a single neuron depicting responses to electrical stimulation at various frequencies, with pulse number held constant. **(C)** IPSC amplitude as a function of frequency, for individual neurons (grey) and the mean of all neurons (blue, n=3). **(D)** Event charge, expressed as a z-score relative to a noise distribution, as a function of frequency. Depicted are individual neurons (grey) and the mean of all neurons (blue, n=3). Green shaded area represents 95% confidence interval for noise distribution.

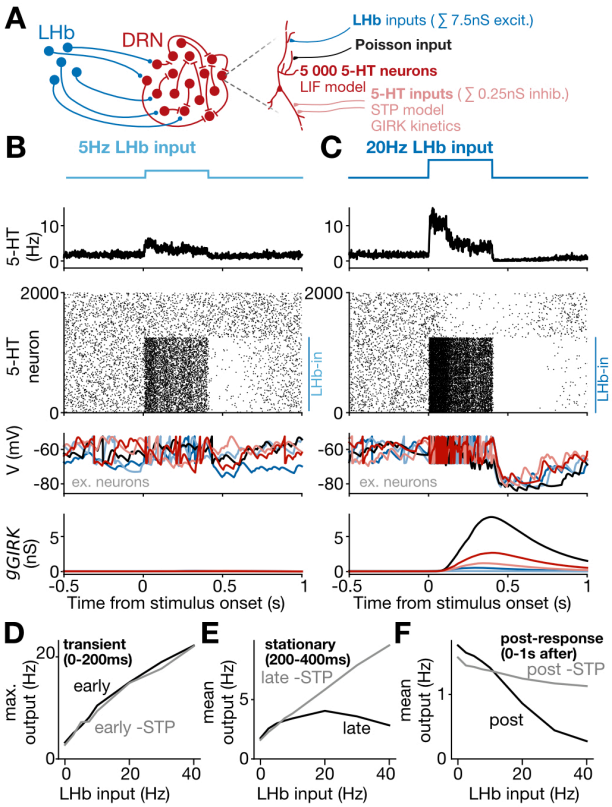

Figure S8: Nonlinear transformation of habenulo-raphe afferents generated by recurrent plasticity rules, with tenfold decrease in recurrent inhibitory connection probability (sum 0.25nS conductance received by each serotonin neuron). **(A)** Schematic of the LIF network model. **(B)** Results of a simulation where a 5Hz step input from LHb was delivered to a subset of serotonin neurons. **(C)** Results of a simulation where a 20Hz step input from LHb was delivered to a subset of serotonin neurons. **(D)** Input-output transformation for the transient (0-200ms) response phase, with (black) and without (grey) STP rules at recurrent serotonergic connections. **(E)** Input-output transformation for the stationary (200-400ms) response phase, with (black) and without (grey) STP rules at recurrent serotonergic connections. **(F)** Input-output transformation for the post-response (0-1s after stimulus) phase, with (black) and without (grey) STP rules at recurrent serotonergic connections.

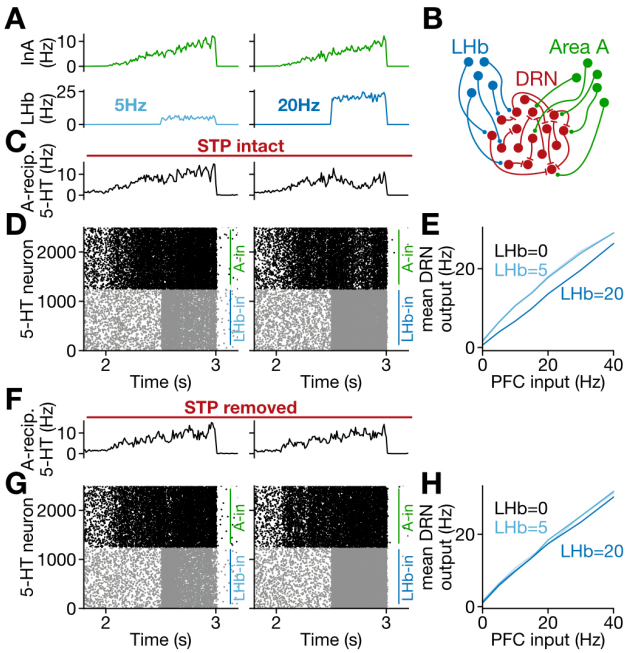

Figure S9: Plasticity-dependent winner-take-all dynamics in raphe, with tenfold decrease in recurrent inhibitory connection probability (sum 0.25nS conductance received by each serotonin neuron). **(A)** Simulations with LHb inputs of either 5Hz (left) and 20Hz (middle) were delivered to serotonin neurons during ramp input from area A. Schematic of LIF network model with two inputs (right). **(B)** Mean responses of serotonin neurons to 5Hz (left) and 20Hz (right) input with STP rules intact. **(C)** Raster plot showing serotonin neuron responses to 5Hz (left) and 20Hz (right) input with STP rules intact. **(D)** Input-output function, for input A, with STP rules intact and coincident LHb input at 0, 5 or 20Hz. **(E)** Mean responses of serotonin neurons to 5Hz (left) and 20Hz (right) input with STP rules removed. **(F)** Raster plot showing serotonin neuron responses to 5Hz (left) and 20Hz (right) input with STP rules removed. **(G)** Input-output function, for input A, with STP rules removed and coincident LHb input at 0, 5 or 20Hz.

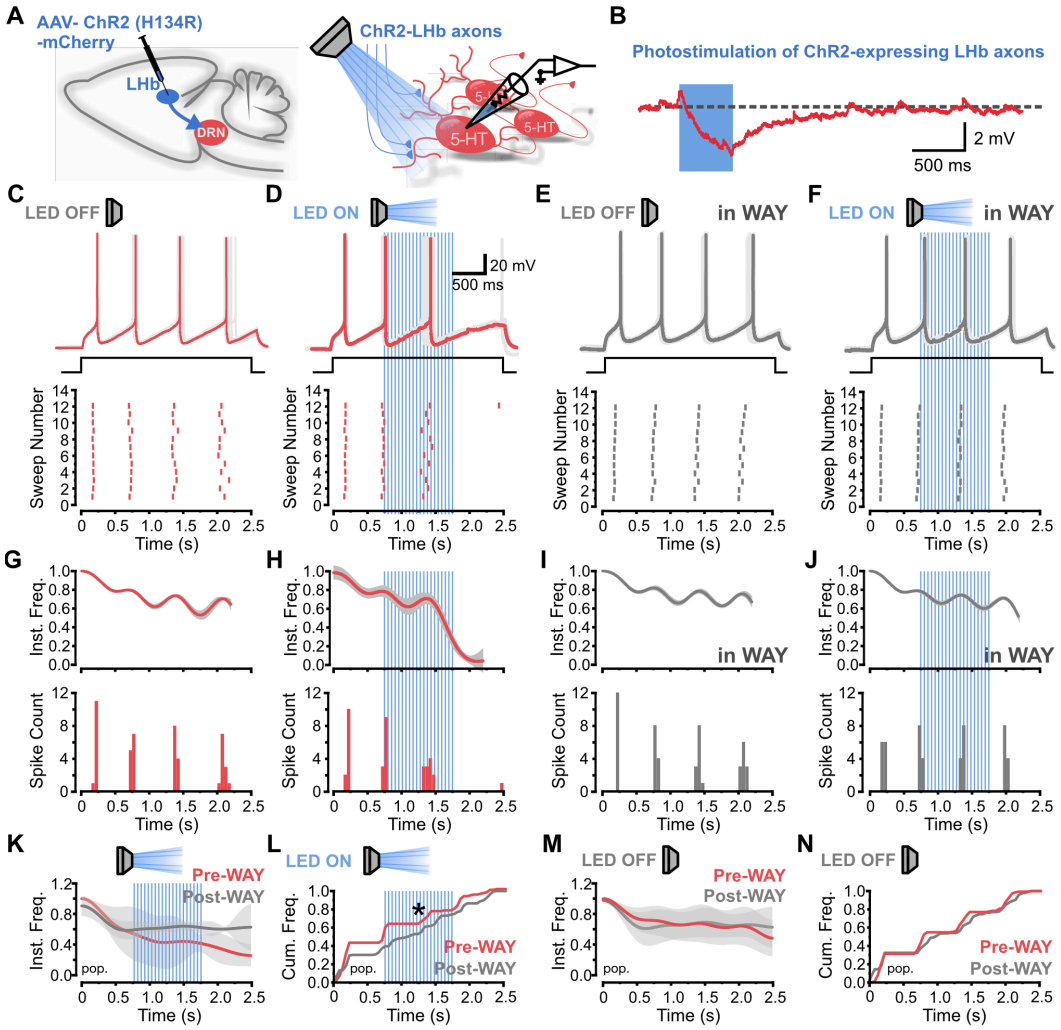

Figure S10: LHb-driven, 5HT1AR mediated, recurrent feedforward modulation of 5-HT firing activity in the DRN. **(A)** Schematic of experimental design. Left, AAV-ChR2(H134R)-mCherry is injected into the LHb. Right, whole-cell recordings from TdT-positive 5-HT neurons. **(B)** LHb-driven heterosynaptic 5HT1AR-mediated potential in SERT-TdT 5-HT neuron. **(C)** Spiking of a 5-HT neuron in response to a 2.5 s current step (scale, 20 mV, 500ms). Below, raster plot of the same 5-HT neuron spiking. **(D)** Spiking of a 5-HT neuron in response to a 2.5 s current step with LED activation of ChR2-expressing LHb terminals in the slice for 1 sec in the middle of the current step. Below, raster plot of the same 5-HT neuron spiking. **(E)** Spiking of a 5-HT neuron in response to a 2.5 s current step in the presence of WAY 100-635. Below, raster plot of the same 5-HT neuron spiking. **(F)** In the presence of WAY 100-635, spiking of a 5-HT neuron in response to a 2.5 s current step with LED activation of ChR2-expressing LHb terminals in the slice for 1 sec in the middle of the current step. Below, raster plot of the same 5-HT neuron spiking. **(G)** Instantaneous frequency line (top) and spike count histogram plots (below) from recording in **C**. **(H)** Instantaneous frequency line (top) and spike count histogram plots (below) from recording in **D**. **(I)** Instantaneous frequency line (top) and spike count histogram plots (below) from recording in **E**. **(J)** Instantaneous frequency line (top) and spike count histogram plots (below) from recording in **F**. **(K)** Instantaneous frequency population plot in pre- and post-WAY recordings with LED stimulation (n=3 neurons, mean +- SE). **(L)** Cumulative frequency population plot in pre- and post-WAY recordings with LED stimulation (3 cells, p = 0.0017, 2-

sample Kolmogorov-Smirnov test). **(M)** Instantaneous frequency population plot in pre- and post-WAY recordings in the absence of LED stimulation (n=3 neurons, mean +- SE). **(N)** Cumulative frequency population plot in pre- and post-WAY recordings in the absence of LED stimulation (3 cells, p = 0.07, 2-sample Kolmogorov-Smirnov test).

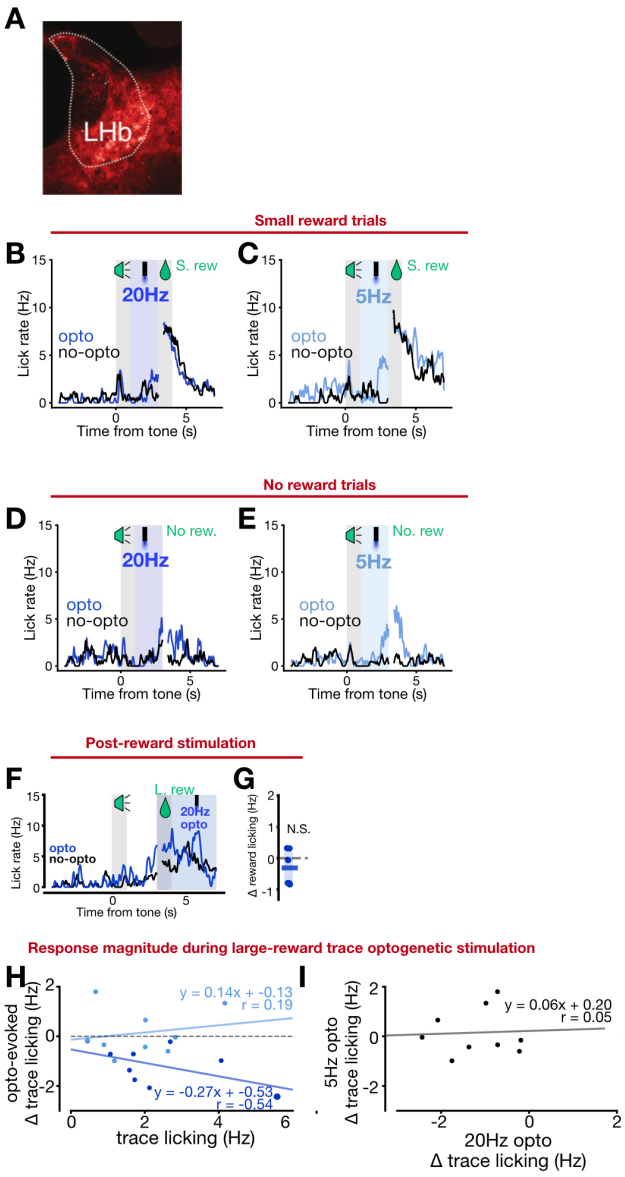

Figure S11: The habenulo-raphe pathway disrupts reward-conditioned responses in a value-dependent manner and does not affect unconditioned response. **(A)** Representative example of LHb injection site. **(B)** Mean licking across all small reward trials for a single mouse depicting control trials (black) or 20Hz optogenetic stimulation trials (blue). **(C)** Mean licking across all small reward trials for a single mouse depicting control trials (black) or 5Hz optogenetic stimulation trials (blue). **(D)** Mean licking across all no reward trials for a single mouse depicting control trials (black) or 20Hz optogenetic stimulation trials (blue). **(E)** Mean licking across all no reward trials for a single mouse depicting control trials (black) or 5Hz optogenetic stimulation trials (blue). **(F-G)** depict post-reward optogenetic stimulation experiments. **(F)** Mean licking across all large reward trials for a single mouse depicting control trials (black) or trials where 20Hz optogenetic stimulation was delivered during the post-reward period (blue). **(G)** Change in post-reward licking during optogenetic stimulation trials, compared to pre-stimulated baseline period (n=6 mice, paired two-sided t-test, unstimulated vs stimulated reward licking). (**H**) Correlation between mean trace licking (large reward trials) and optogenetic effect size for 20Hz stimulation (dark blue) and 5Hz stimulation (light blue) for trace stimulation during large reward trials. (**I**) Correlation between effect size for 20Hz stimulation and 5Hz stimulation for trace stimulation during large reward trials.